Modeling and energetics of tidally generated wave trains in the Lombok Strait: Impact of the Indonesian Throughflow

H. Aiki,[1] J. P. Matthews,[2,3] and K. G. Lamb[4]

Received 14 August 2010; revised 1 November 2010; accepted 2 December 2010; published 22 March 2011.

[1] This study investigates the possible impact of the Indonesian Throughflow (ITF) on tidally generated internal waves in Lombok Strait and examines the energetics of these disturbances. Using a two-dimensional nonhydrostatic numerical model which takes into account the variable width of the strait region, two main experiments have been performed, one without and one with an idealized ITF component in the upper layer flowing southward toward the Indian Ocean. These correspond to conditions in boreal winter and summer, respectively. Both experiments show trains of internal solitary-like gravity waves (ISWs). Overall, ISWs are more numerous on the north side of the sill where the narrower channel in effect amplifies the disturbances. In both experiments about 3.9 GW of energy is injected into barotropic and baroclinic tidal currents, of which about 2.6 GW is radiated away by internal gravity waves. The ITF regulates the way that the radiated energy is partitioned between the two sides of the sill. Without the ITF (boreal winter), the northward radiated energy flux is greater in magnitude than that radiated to the south. However, when the ITF is present (boreal summer), the northward radiated energy flux is smaller in magnitude than that radiated to the south. This result is obtained by diagnosing the flux of the Montgomery potential which can take into account the effect of finite amplitude waves and also offers a simple and robust energy diagnosis in the presence of time mean flows.

Citation: Aiki, H., J. P. Matthews, and K. G. Lamb (2011), Modeling and energetics of tidally generated wave trains in the Lombok Strait: Impact of the Indonesian Throughflow, *J. Geophys. Res.*, *116*, C03023, doi:10.1029/2010JC006589.

1. Introduction

[2] Tidal mixing in the ocean can be attributed to a series of nonhydrostatic processes, such as Kelvin-Helmholtz instability, hydraulic-jump-like overturning, internal swash/surf action on a sloping bottom, and the shoaling of internal solitary-like gravity waves (ISWs) [cf. *Moum et al.*, 2008]. Recent oceanographic studies have paid considerable attention to tidal mixing in the Indonesian Seas, as this process changes the vertical structure of the Indonesian Throughflow (ITF) and thereby affects heat transport between the Pacific and Indian Oceans [cf. *Ffield and Gordon*, 1996; *Koch-Larrouy et al.*, 2008; *Robertson and Ffield*, 2008; *Robertson*, 2010].

[3] Lombok Strait (LS) is one of the major passages for the ITF, and is known to have a tall, sharply defined sill which induces strong tidal flows of ±3.5m/s [*Murray and Arief*, 1988]. Figure 1a depicts an ERS-1 Synthetic Aperture Radar (SAR) image over the LS region, acquired at 0232 UTC on 23 April 1996 (as used by *Susanto et al.* [2005]), which shows two sets of wave arcs (A and B) in the Java Sea and one wave arc (C) in the Indian Ocean, all of which are generated at the sill by the M_2 tide. The leading wave arc is followed by a train of waves 2–7 km in length, which are the surface expressions of ISWs. Wave trains of this type represent some of the largest nonhydrostatic phenomena in the ocean [cf. *Osborne and Burch*, 1980; *Helfrich and Melville*, 2006] and highlight the differences between the dispersion relations of hydrostatic and nonhydrostatic internal gravity waves (Figure 2) [*Lamb*, 1994].

[4] Recently *Matthews et al.* [2011, hereafter Ma11] analyzed the statistics of satellite SAR images gathered over the LS region, and compared the occurrences of wave trains propagating northward and southward from the sill. They found it necessary to recognize two main classes of high-frequency nonlinear internal waves in the LS region. The first of these represents ISWs generated as a result of flow enhancement caused by the topography of the sill, and which radiate outward in uniform concentric arcs, whereas the second class includes irregular, braided disturbances that are closely associated with and may possibly be released from the frontal boundaries of warm water intrusions that advance southward into the Indian Ocean. In the present

[1] Research Institute for Global Change, Japan Agency for Marine-Earth Science and Technology, Yokohama, Japan.
[2] Environmental Satellite Applications, Anglesey, Wales, UK.
[3] Department of Geophysics, Kyoto University, Kyoto, Japan.
[4] Department of Applied Mathematics, University of Waterloo, Waterloo, Ontario, Canada.

0148-0227/11/2010JC006589

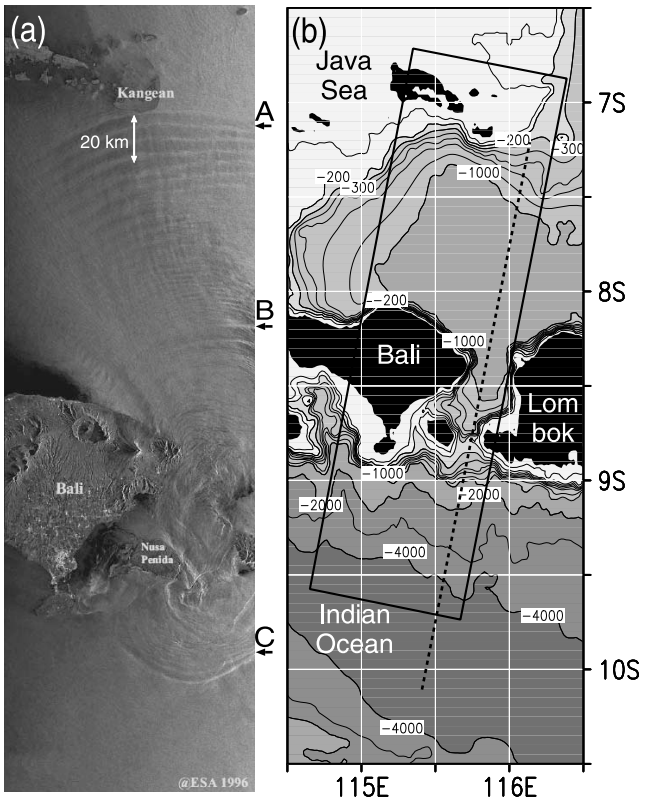

Figure 1. (a) ERS-1 SAR image over Lombok Strait acquired at 0232 UTC on 23 April 1996 (adapted from *Susanto et al.* [2005]). (b) Bottom topography (m) with the solid box representing the region covered by Figure 1a and the dashed line representing the main axis of the strait along which the numerical model is configured.

numerical study, we focus on the first class of internal waves (namely the arc-like ISWs radiating uniformly away from the sill) and do not consider the second class. From the analysis of a multiyear mean data set based on 932 archived SAR scenes, Ma11 found that the ISW trains of the first class were detected more frequently on the Java Sea side, propagating northward. This directional asymmetry was particularly well defined during the boreal winter period of the northwest monsoon (roughly December–May). During boreal summer, the period of the southeast monsoon (roughly June–November), the irregular waves of the second class were identified in abundance on the Indian Ocean side, propagating to the south and west. Ma11 considered this seasonal variability to reflect the seasonal behavior of the ITF itself, which has a tendency to weaken during the boreal winter and flow strongly southward during the boreal summer [cf. *Masumoto and Yamagata*, 1996; *Sprintall et al.*, 2009]. A related characteristic of the ITF is that its southward transport is weakened during El Niño years and enhanced during La Niña years [*England and Huang*, 2005]. We recognize that the satellite-based LS internal wave results reported by Ma11 have not to date been independently confirmed by comparison, for example, with detailed in situ observations gathered by moorings. One of the aims of our study, therefore, is to examine the internal wave seasonality obtained by Ma11 in the light of results derived from our numerical study and to suggest where further experimental work is required.

[5] A number of numerical studies for ISW trains have been presented for various regions of the global ocean, including Georges Bank, the Strait of Messina, the Gulf of Oman, the South China Sea, and the Yellow Sea etc. [*Lamb*, 1994; *Brandt et al.*, 1997; *Small and Martin*, 2002; *Warn-Varnas et al.*, 2005, 2010; *Chao et al.*, 2007; *Zheng et al.*, 2007; *Shen et al.*, 2009; *Buijsman et al.*, 2010]. These studies used a two-dimensional nonhydrostatic model, except for *Shen et al.* [2009] who use a three-dimensional model, in the vertical plane and assume no variation in the direction normal to the plane. This assumption was also used by *Ningsih et al.* [2008] who presented model results in an early attempt to simulate tidally generated wave trains in LS. Although they used the World Ocean Atlas to demonstrate the impact of the seasonal variability of the thermocline on tidal internal waves, the lack of detailed observations of the spatial distributions of temperature and salinity in this region makes it difficult to pursue this approach further. On the other hand, to our knowledge, there has been no numerical study which (1) takes into account the variable width of the LS region in a two-dimensional nonhydrostatic model, (2) investigates the impact of the ITF on tidally generated wave trains, and (3) considers the energetics of tidal internal waves in LS. These are the main subjects of the present study. We also address fundamental

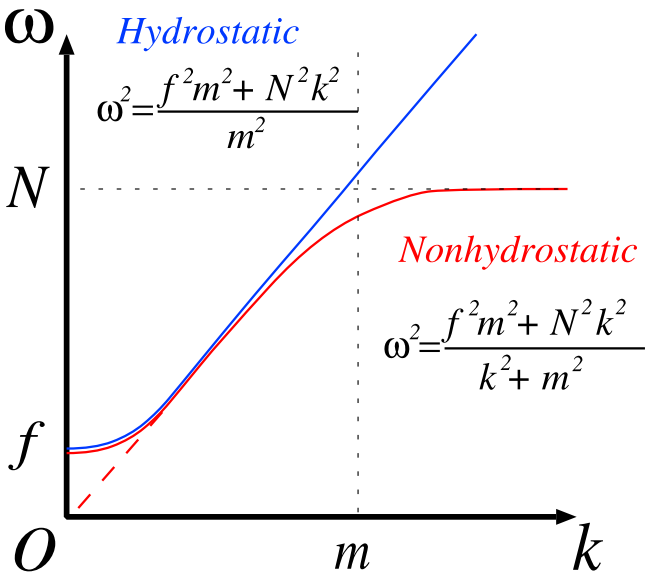

Figure 2. Hydrostatic (blue) and nonhydrostatic (red) dispersion relations of internal gravity waves in linear theory with the symbols ω, N, and f representing wave, buoyancy, and Coriolis frequencies and k and m representing the horizontal and vertical wavenumbers. The dashed red line near the origin indicates the dispersion relation of waves in a nonrotating frame.

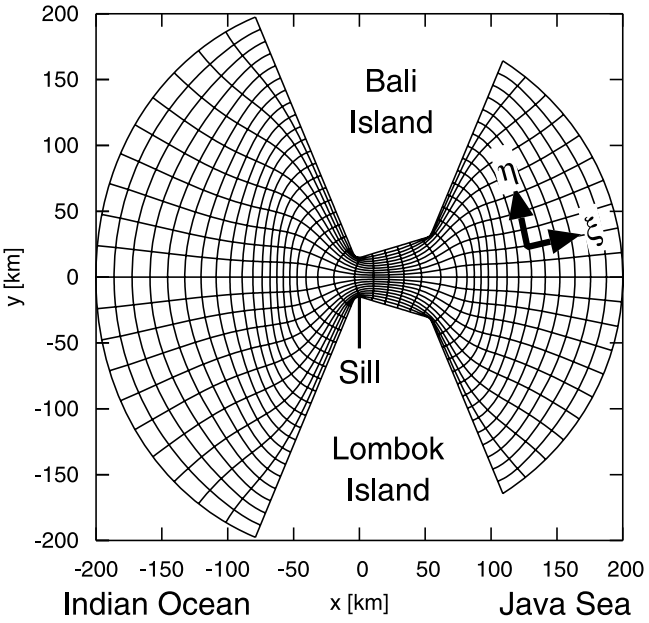

Figure 3. Curvilinear orthogonal coordinates for the water regions of Lombok Strait with idealized coastlines.

aspects of the energy diagnosis of internal waves in the presence of time mean flows.

2. Model

[6] We consider fluid motion in a vertical plane aligned along the main axis of LS (the dashed line in Figure 1b). The model strait (hereafter channel) consists of a realistic bottom profile and an idealized width profile as follows. The bottom depth is given by the General Bathymetric Chart of the Ocean. The channel width $L[x](>0)$ is idealized in the form shown in Figure 3. The sill is located at $x = 0$ km where the water depth and the channel width are 270 m and 30 km, respectively.

[7] The model is based on the two-dimensional equations in the vertical plane derived by assuming radial propagation of waves away from the sill and taking the width average of the three-dimensional nonhydrostatic incompressible Boussinesq equations (Appendix A). The equations can be written in the form

$$\rho_0(U_t + UU_x + wU_z) = -p_x + D^U, \tag{1}$$

$$\rho_0(w_t + Uw_x + ww_z) = -p^{\mathbf{n}}_z + D^w, \tag{2}$$

$$(LU)_x + (Lw)_z = 0, \tag{3}$$

$$\rho_t + U\rho_x + w\rho_z = D^\rho, \tag{4}$$

where $U[x, z, t]$ and $w[x, z, t]$ are the northward and upward components of velocity and ρ_0 and $\rho[x, z, t]$ are the reference and model density of sea water. See Table 1 for an explanation of the symbols used in the present paper. The term $p[x, z, t] \equiv p^{\mathbf{s}}[x, t] + p^{\mathbf{h}}[x, z, t] + p^{\mathbf{n}}[x, z, t]$ is the sum of sea surface pressure (SP), hydrostatic pressure (HP, $p^{\mathbf{h}} \equiv \int_z^0 \rho g dz$ with sea surface being at $z = 0$ and $g = 9.8\text{m}/s^2$ being the gravitational acceleration), and nonhydrostatic pressure (NP). The last of these quantities is necessary to produce trains of ISWs. The D (mixing) terms are discussed two paragraphs below. The continuity equation (3) takes into account the variable width of the channel, so that our strategy is analogous to that used by *Brandt et al.* [1997] who presented a two-layer nonhydrostatic model for the Strait of Messina. As with *Brandt et al.* [1997], we do not consider the rotation of the Earth, which is a limitation arising from setting the channel width in the two-dimensional model in the vertical plane. All equations in the present manuscript assume a rigid sea surface, which facilitates the derivation of the energy equations (the fact that the model we use for our numerical experiments has a free surface does not compromise the results of our energy diagnosis, see Appendix B).

[8] The set of equations (1)–(4) is discretized in (x, z) coordinates and stepped forward using the numerical code of *Aiki and Yamagata* [2004] and *Menesguen et al.* [2009]. The horizontal grid spacing is 140 m. A total water depth of 4200 m is covered by 80 depth levels with a uniform vertical grid spacing of 10 m for the top 600 m. Grid spacings at greater depth increase monotonically.

[9] The terms D^U, D^w, and D^ρ in (1)–(4) represent the subgrid-scale mixing of U, w, and ρ, respectively. The subgrid-scale horizontal mixing is parameterized by the standard *Smagorinsky* [1963] scheme with a nondimensional coefficient of 0.1 after squaring, which is a value often used in high-resolution coastal ocean models. The Prandtl number is set to unity as the horizontal mixing parameter. The subgrid-scale vertical mixing is parameterized by setting the hyperviscosity to $-1.0\text{m}^4/s$ and the hyperdiffusivity to $-0.01\text{m}^4/s$, which suggest 10^{-4} (1/s) and 10^{-6} (1/s) for the damping rates of grid noise in velocity and tracer fields, respectively. The bottom friction is parameterized using a quadratic stress law with a standard nondimensional drag coefficient of 0.0025.

2.1. Forcing

[10] The model is forced by the barotropic volume fluxes through the open boundaries located at $x = \pm 200$ km. The boundary fluxes oscillate at the M_2 tidal period (12.42 h $\equiv \tau$). The amplitude of the fluxes is based on the output of a 1/24° × 1/24° resolution barotropic inversion model for the North Australian region (Egbert and Erofeeva, http://volkov.oce.orst.edu/tides/region.html). This inversion model gives barotropic volume transports of 8.0, 3.7, 2.7, and 1.6Sv (1Sv = 10^6 m^3/s) for the M_2, S_2, K_1, O_1 tides through LS. The simplest way to reproduce 8.0Sv for the barotropic tidal transport "at the sill" in our model is to set the open boundary fluxes at 8.0Sv with no phase difference between the fluxes on the two sides of the sill. This approach has been conventionally adopted in the modeling of tidal internal waves with a rigid sea surface. Although our model has a free sea surface, we follow the above approach for simplicity. The barotropic tidal forcing of 8.0Sv results in a barotropic (i.e., depth averaged) velocity over the sill of 0.99m/s. A radiation boundary condition for the baroclinic part of the flow is given at the open boundaries.

Table 1. List of Symbols

Symbol	Description
(x, y)	Cartesian coordinates in the horizontal plane
(ξ, η)	curvilinear orthogonal coordinates in the horizontal plane
(h^{ξ}, h^{η})	positive scale factors in (ξ, η) coordinates
ξ^s	position of the sill of Lombok Strait
η^l	position of the coastline of the Lombok island
η^b	position of the coastline of the Bali island
$L \equiv \int_{\eta^l}^{\eta^b} h^{\eta}\, d\eta$	channel width
H	bottom depth
$\widetilde{A} \equiv \int_{\eta^l}^{\eta^b} Ah^{\eta} d\eta / L$	width average along the line of a fixed ξ (A is an arbitrary quantity)
$A'' \equiv A - \widetilde{A}$	deviation from the width average (compared at fixed ξ, $\widetilde{A''} \equiv 0$)
$\overline{A}$	Eulerian time mean
$A' \equiv A - \overline{A}$	deviation from the Eulerian time mean ($\overline{A'} \equiv 0$)
(u, v)	horizontal components of velocity in (x, y) coordinates
(U, V)	horizontal components of velocity in (ξ, η) coordinates
w	vertical component of velocity
$(\widetilde{U}, \widetilde{w})$	components of width-averaged velocity in (ξ, z) and (x, z) coordinates
$(\widetilde{U}^{\mathbf{bt}}, \widetilde{w}^{\mathbf{bt}})$	barotropic component of $(\widetilde{U}, \widetilde{w})$
$\widetilde{U}^{\mathbf{bt}} \equiv \int_{-H}^{0} \widetilde{U} dz / H$	barotropic (i.e., depth averaged) component of $\widetilde{U}$
$\widetilde{w}^{\mathbf{bt}} \equiv (z/H)\widetilde{U}H_x$	barotropic component of $\widetilde{w}$: $(L\widetilde{U}^{\mathbf{bt}})_x + (L\widetilde{w}^{\mathbf{bt}})_z = 0$
$(\widetilde{U}^{\mathbf{bc}}, \widetilde{w}^{\mathbf{bc}})$	baroclinic component of $(\widetilde{U}, \widetilde{w})$
$\widetilde{U}^{\mathbf{bc}} \equiv \widetilde{U} - \widetilde{U}^{\mathbf{bt}}$	baroclinic (i.e., residual) component of $\widetilde{U}$
$\widetilde{w}^{\mathbf{bc}} \equiv \widetilde{w} - \widetilde{w}^{\mathbf{bt}}$	baroclinic component of $\widetilde{w}$: $(L\widetilde{U}^{\mathbf{bc}})_x + (L\widetilde{w}^{\mathbf{bc}})_z = 0$
ρ	total density of seawater
ρ_0	reference density of seawater
g	gravity acceleration
$p^{\mathbf{s}}$	sea surface pressure (SP)
$p^{\mathbf{h}} \equiv \int_z^0 g\rho dz$	hydrostatic pressure (HP)
$p^{\mathbf{n}}$	nonhydrostatic pressure (NP)
$p \equiv p^{\mathbf{s}} + p^{\mathbf{h}} + p^{\mathbf{n}}$	total pressure
$M \equiv p^{\mathbf{s}} + p^{\mathbf{h}} + \rho gz$	Montgomery potential (MP)
$\rho^{\mathbf{z}}$	density of the background stratification $\rho_x^{\mathbf{z}} = \rho_t^{\mathbf{z}} = 0$
$\rho^{\mathbf{a}} \equiv \rho^{\mathbf{a}} - \rho^{\mathbf{z}}$	density anomaly
$\rho^{\mathbf{a}} gz$	potential energy anomaly (PEA)
$p^{\mathbf{hz}} \equiv \int_z^0 g\rho^{\mathbf{z}}\, dz$	hydrostatic pressure based on background stratification $p_x^{\mathbf{hz}} = p_t^{\mathbf{hz}} = 0$
$p^{\mathbf{ha}} \equiv p^{\mathbf{h}} - p^{\mathbf{hz}}$	hydrostatic pressure anomaly (HPA) $p_z^{\mathbf{ha}} = -g\rho^{\mathbf{a}}$
$\rho^{\mathbf{i}}$	initial density
H_1	reference thickness of upper layer
$\tau \equiv 12.42$ h	period of M_2 tide

2.2. Initial Condition

[11] The initial density field is set by a quartic exponential vertical profile: $\rho^{\mathbf{i}} \equiv \rho_0 - \Delta\rho \exp[-0.7(z/H_1)^4]$ where $\Delta\rho$ is the density difference across the thermocline, and $H_1 > 0$ is the upper layer reference thickness. (Although the standard Gaussian function (i.e., $\exp[-z^2]$) might be closer to the observed density profile, we used the quartic Gaussian function (i.e., $\exp[-z^4]$) so that the stratification can be regarded as a two-layer model, which helps simplify the vertical profile of the model ITF (i.e., a vertically uniform southward flow in the upper layer and no flow in the lower layer, see section 3.2). The qualitative nature of the model result will be unchanged whichever of the standard and quartic Gaussian functions is used.) We set $H_1 = 150$ m based on the observed velocity profile of the ITF passing through LS [*Sprintall et al.*, 2009] and the thermocline depth in the World Ocean Atlas of 2005. We then choose a value of $\Delta\rho = 3.50\text{kg/m}^3$ so that the linear long wave speed of the first baroclinic mode becomes 1.93 m/s on the Java Sea side where the maximum bottom depth is 1400 m and 2.02 m/s on the Indian Ocean side where the maximum bottom depth is 4200 m. These values are close to an observed propagation speed of 2.01m/s = 90 km/τ which is estimated from the separation distance of wave arcs A and B in Figure 1a. The observed propagation speed is a nonlinear propagation speed and hence larger than the linear long wave speed. There are buffer zones next to the open boundaries where the model density ρ is restored to the initial density $\rho^{\mathbf{i}}$ within a time scale of τ throughout the time integration.

3. Experiments

[12] We have performed two main experiments, one without and one with an idealized ITF, corresponding to conditions in boreal winter and summer (or in El Niño and La Niña years), respectively. Such sensitivity experiments have begun to attract attention in recent numerical studies of ISWs in the other regions of the world's oceans, such as that of *Warn-Varnas et al.* [2010] who investigated the possible impact of the variability of the Kuroshio current on tidally generated ISWs in the South China Sea. For each of our two experiments the model was integrated for 25 M_2 cycles until a statistically equilibriated state was achieved, although the basic features of the tidal waves were obtained within a few M_2 cycles of integration.

3.1. Case Without the ITF (Boreal Winter)

[13] This experiment was started from an initial condition of no motion. The barotropic component of U over the sill is indicated by the black line in Figure 4a, where the maximum southward and northward tides occur at $t = 24.25\tau$ and 24.75τ, respectively.

[14] Snapshots of ρ and U at maximum southward and northward barotropic tidal currents are plotted in Figure 5. On the Java Sea side the thermocline has depressions A and

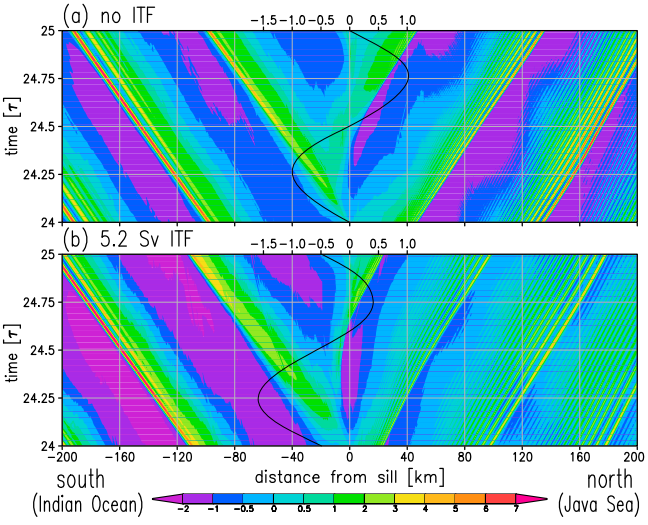

Figure 4. Time series of the combined width and depth integral of the potential energy anomaly (PEA) $L\int_{-H}^{0}(\rho - \rho^{\mathbf{i}})gzdz$ (color, 10^{12} J/m) and the depth average of the northward component of velocity at the sill $\int_{-H}^{0} Udz/H$ at $x = 0$ km (black line, m/s) during the 25th M_2 cycle in the experiments (a) without the ITF and (b) with it.

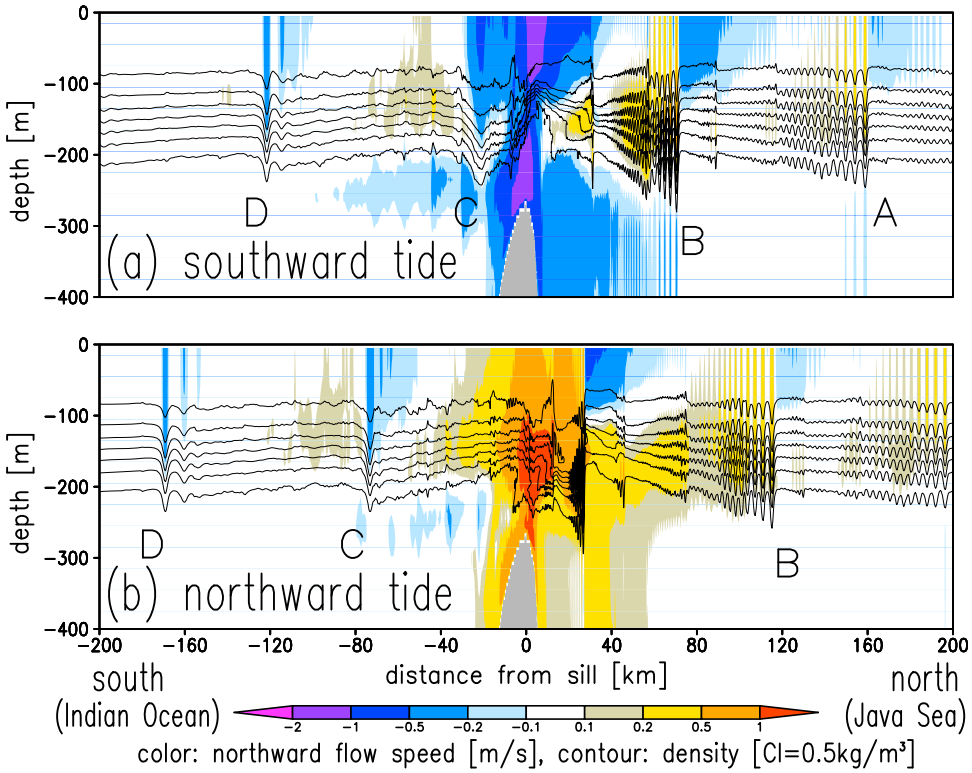

Figure 5. The result of an experiment without the ITF. Distributions of the northward component of velocity (color) and density (contours) at the maximum (a) southward and (b) northward barotropic tides in the 25th M_2 cycle (i.e., t = 24.25 and t = 24.75 in Figure 4, respectively).

B which are generated by a northward tide over the sill. The leading edge of each depression is followed by a wave train with waves about 4 km in wavelength which is in the range of the observed wavelengths. The thermocline displacement gradually decreases as waves propagate away from the sill. However, Figure 4a shows that the combined width and depth integral of the potential energy anomaly (PEA = $(\rho - \rho^{i})gz$) for each wave increases slightly during propagation, suggesting that energy is still being transferred from internal tides to ISWs. (This transfer from low- to high-frequency internal waves is not isolated in the energy diagnosis in section 4.) The leading wave of each wave train on the Java Sea side propagates at 1.97 m/s (in regions between x = 40 km and x = 160 km), while that on the Indian Ocean side propagates at 2.11 m/s. These speeds are slightly faster than the linear long wave speed. The slight deceleration in the regions of x > 160 km in Figure 4a reflects the shoaling of waves as they approach the northern end of the basin (Figure 1b).

[15] These topographically generated wave trains are more pronounced on the Java Sea side of the sill. A large number of ISWs form in the northward propagating wave trains, which is consistent with observations [*Mitnik et al.*, 2000; *Susanto et al.*, 2005; Ma11]. In the south only a single ISW is generated, which is generally more difficult to identify as an ISW event in remote sensing imagery. In order to examine the reason for this directional asymmetry, we performed a supplementary experiment with exactly the same settings as the original experiment except that a uniform channel width of 30 km was used. (We also used a uniform bottom depth of 1400 m in regions of x > 100 km in order to eliminate southward wave reflections caused by the northward shoaling of high-amplitude waves.) In this experiment only the asymmetric bottom topography of LS

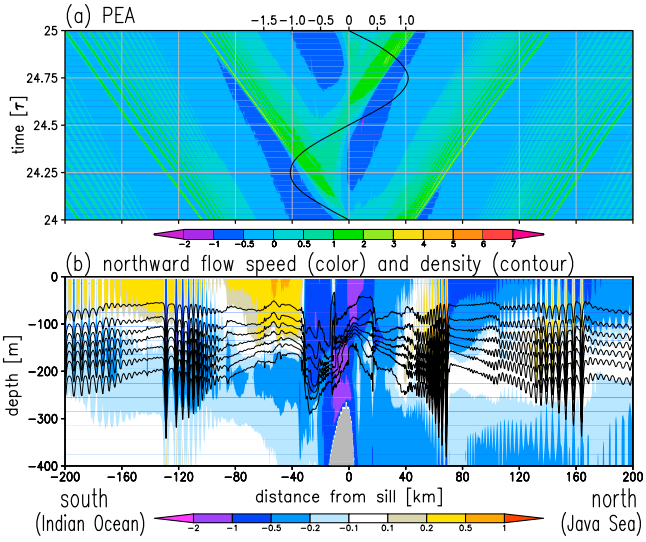

Figure 6. (a) Same as Figure 4a and (b) same as Figure 5a except for the result of an experiment using a uniform channel width of 30 km (also a uniform bottom depth of 1400 m has been used in regions of x > 100 km).

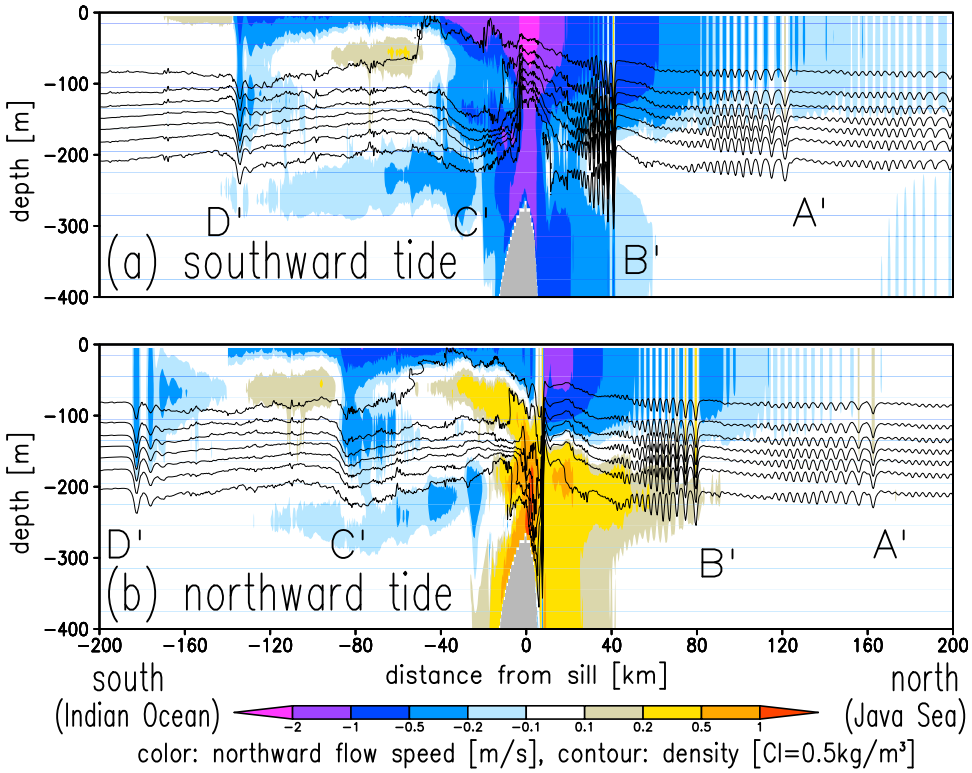

Figure 7. Same as Figure 5 except for the result of an experiment with the ITF.

is capable of causing an asymmetry between wave trains generated north and south of the sill. The result in this case is that more than ten ISWs develop within each wave train on both the Indian Ocean side and the Java Sea side (Figure 6). The amplitude of the depressions is about 100 m (trough-to-peak) on both sides of the sill, indicating that flows and waves are enhanced in this uniformly narrow channel. On the other hand, in spite of the increased wave amplitude, the width integral of the PEA shown in Figure 6a is much smaller than that in Figure 4a. These results suggest the importance of taking into account the variable width of the LS region for reproducing the observed asymmetry of the wave trains. The narrow channel width in the regions between $x = 0$ and 50 km (Figure 3) of the original experiment induces a megaphone-like amplification of the northward propagating depressions, resulting in the formation of many ISWs in each wave train.

3.2. Case With the ITF (Boreal Summer)

[16] This experiment introduces a vertically uniform southward ITF in the upper 150 m layer, by changing both the initial and open boundary conditions. This current lies above the sill which is at a depth of 270 m. The magnitude of the ITF is set to 5.2 Sv, which is twice the observed multiyear mean volume transport of 2.6 Sv through LS between 2004 and 2006 [*Sprintall et al.*, 2009]. The seasonal difference in the observed Lombok ITF is about 5.0 Sv in 2005 and 2006, but is smaller in 2004 [see *Sprintall et al.*, 2009, Figure 9a]. The phase of the barotropic tide is unchanged as shown by the black line in Figure 4b.

[17] The northward propagating wave trains are simulated again but with considerably smaller amplitudes (trough-to-peak height is about 20 m in regions around $x = 150$ km, see A′ in Figure 7a) than the corresponding events in the experiment without the ITF where the trough-to-peak height is about 30 m in regions around $x = 150$ km (see B in Figure 5a). The decrease of wave amplitudes can be seen in the distributions of the PEA (Figure 4) and, as Ma10 show, in the horizontal divergence of velocity, which has clear implications for the detection of the surface signals by satellite-borne SARs. In this "ITF on" experiment, the wave trains have an increased wave length of about 6 km. The depressions A′ and B′ are located closer to the sill, owing to the strong counter advection by the ITF near the sill. Once the northward propagating waves reach regions that are sufficiently removed from the sill ($x > 80$ km), they propagate at speeds that are somewhat slower than those in the first experiment without the ITF. On the other hand, the presence of the ITF speeds up the southward propagating waves on the Indian Ocean side of the sill (Figure 4b). Two to three ISWs are formed in each wave train.

[18] Concerning the Doppler shift by the ITF, below we compare two types of length scale of tidal internal waves. The first length scale is the separation distance between the leading edge of depressions (about 90 km), which can be explained by the Doppler shift. In fact our experiment with the ITF shows that the separation distance is decreased upstream the sill (the Java Sea side) and increased downstream the sill (the Indian Ocean side). The second length scale is the wavelength of each ISW (about 5 km), which cannot be explained by the Doppler shift. In fact our

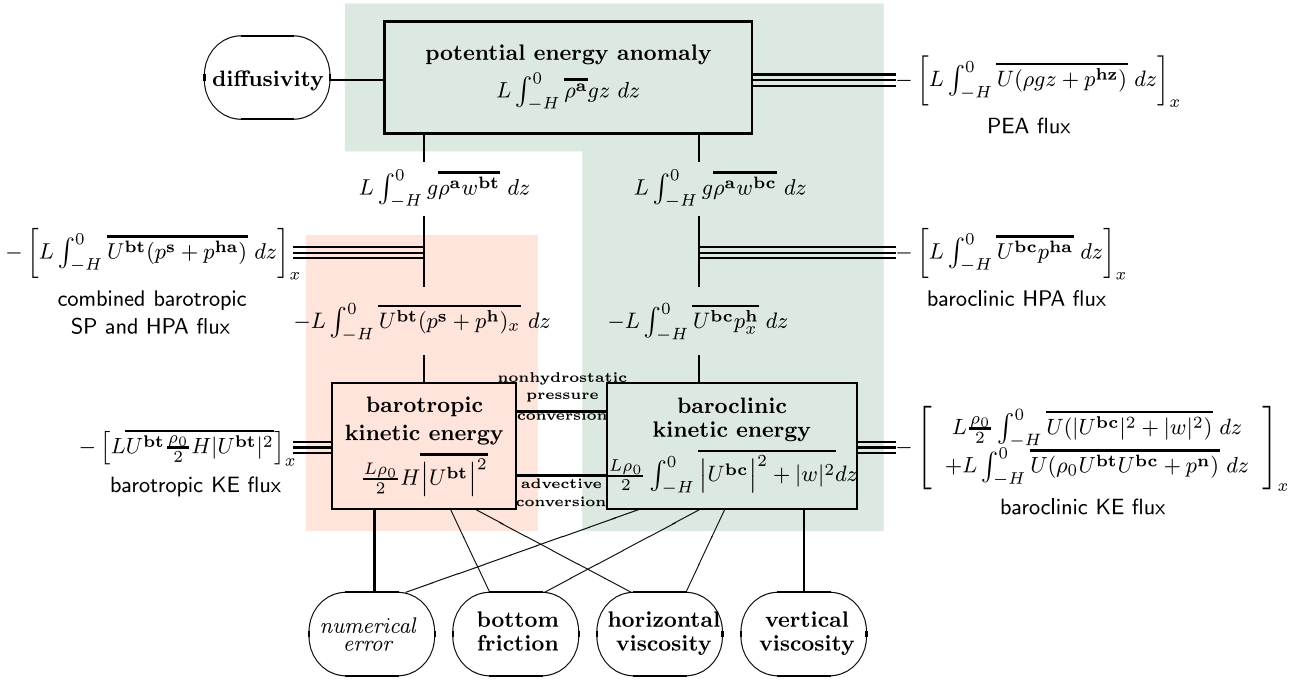

Figure 8. Energy diagram based on (C7) and (C12)–(C15) with the overbar symbol representing the Eulerian time average. The triple lines indicate energy fluxes through the lateral boundaries of the analysis domain. The red and green shaded boxes represent the definitions of barotropic and baroclinic energies used in previous studies. See section C1.

experiment with the ITF shows that the wavelengths of the ISWs are increased upstream of the sill (the Java Sea side). This is not necessarily surprising as the wavelength of ISWs is set by the wave amplitude, stratification, and the vertical shear of the ITF [cf. *Miyata*, 1985; *Brandt et al.*, 1997].

4. Energy Diagnosis

[19] The purposes of the energy diagnosis are to (1) quantify the rate at which wave energy is radiated from the LS region and (2) distinguish the energetics of waves and time mean flows.

[20] The barotropic and baroclinic components of U are defined by $U^{\mathbf{bt}} \equiv \int_{-H}^{0} U dz/H$ and $U^{\mathbf{bc}} \equiv U - U^{\mathbf{bt}}$, respectively. Then the kinetic energy (KE) in each vertical column can be separated into $\frac{\rho_0}{2}H|U^{\mathbf{bt}}|^2$ (barotropic KE) and $\frac{\rho_0}{2}\int_{-H}^{0} |U^{\mathbf{bc}}|^2 + |w|^2 dz$ (baroclinic KE) where $H[x]$ is the bottom depth [*Holland*, 1975; *Baines*, 1982; *Cummins and Oey*, 1997; *Niwa and Hibiya*, 2004; *Carter et al.*, 2008; *Aiki et al.*, 2011]. For simplicity we do not separate $|w|^2$ into barotropic and baroclinic component as our numerical results indicate that $|w|^2$ is 2 orders of magnitude smaller than the other kinetic energy terms and hence insignificant.

[21] In order to derive an equation for the PEA, we decompose density into that associated with the background stratification and with the anomaly: $\rho[x, z, t] \equiv \rho^{\mathbf{z}}[z] + \rho^{\mathbf{a}}[x, z, t]$ where the profile of $\rho^{\mathbf{z}}$ is arbitrary. The density equation (4) becomes

$$\rho^{\mathbf{a}}_t + U\rho^{\mathbf{a}}_x + w\rho^{\mathbf{a}}_z + w\rho^{\mathbf{z}}_z = D^{\rho}. \tag{5}$$

By using (1)–(3) and (5) one can derive equations for the barotropic and baroclinic KEs and PEA. The resulting energy budget is illustrated by the diagram in Figure 8 where the buoyancy conversion term $g\rho^{\mathbf{a}}w$ is decomposed into terms associated with the barotropic and baroclinic components of velocity defined by $w^{\mathbf{bt}} \equiv U^{\mathbf{bt}} H_x z/H$ and $w^{\mathbf{bc}} = w - w^{\mathbf{bt}}$ (section C1). The symbols $p^{\mathbf{hz}}(\equiv \int_z^0 g\rho^{\mathbf{z}} dz)$ and $p^{\mathbf{ha}}(\equiv p^{\mathbf{h}} - p^{\mathbf{hz}})$ represent the hydrostatic pressure (HP) associated with the background stratification and that related to the anomaly, respectively (the latter of which is hereafter abbreviated as HPA). The energy budget is diagnosed by setting $\rho^{\mathbf{z}} = \rho^{\mathbf{i}}$ and taking a volume integral in the region between $x = \pm 120$ km. In the following we use the word 'flux' to indicate the net energy flux through the lateral boundaries at $x = \pm 120$ km. The diagnosis is also based on a time average for the last five M_2 cycles of the integration period. We use the overbar and prime symbols to represent the Eulerian time mean and perturbation components, respectively, so that

$$A[x, z, t] = \overline{A}[x, z] + A'[x, z, t], \tag{6}$$

for an arbitrary quantity $A[x, z, t]$.

4.1. Case Without the ITF (Boreal Summer)

[22] The energy cycle starts from the combined barotropic SP and HPA flux through the lateral boundaries at $x = \pm 120$ km. This represents some 3.86 GW (Figure 9a, 1 GW = 10^9 W). About three quarters of this is converted into PEA (2.96 GW), with the rest used to maintain the budget of barotropic KE (0.89 GW). The barotropic and baroclinic buoyancy terms roughly offset each other (+2.96 GW and

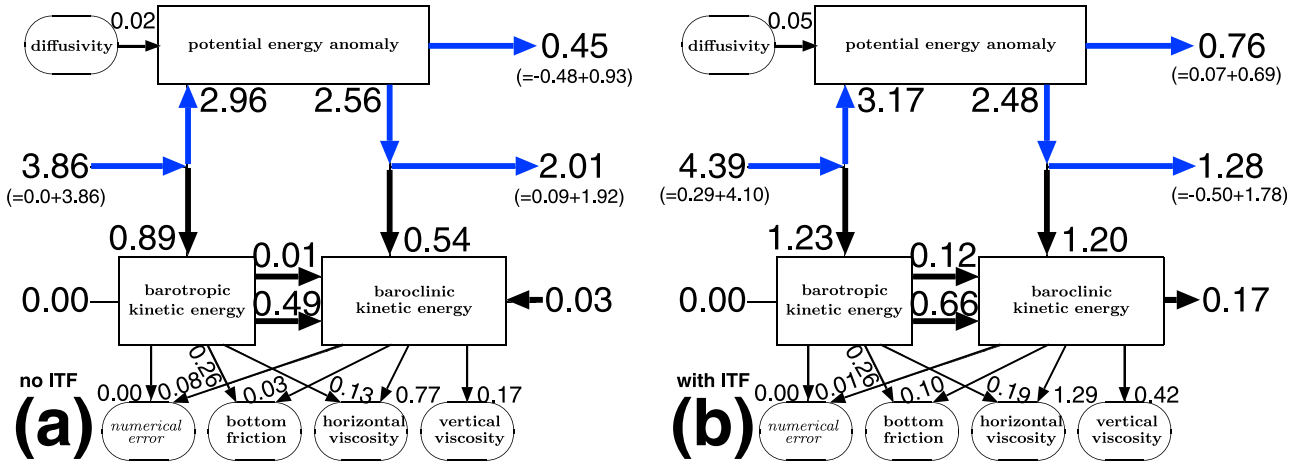

Figure 9. Energy conversion rates (GW) based on the energy diagram of Figure 8 in the experiments (a) without the ITF and (b) with it. The values are obtained by taking a volume integral in the region between $x = \pm 120$ km with a time average for the last five M_2 cycles of the integration period. The residual of the energy budget of each box represents the tendency. For each of the combined barotropic SP and HPA flux, the baroclinic HPA flux, and the PEA flux, contributions from the mean correlation and the wave correlation are computed (i.e., $\overline{UA} = \overline{U}\,\overline{A} + \overline{U'A'}$), as shown by the first and second values in each bracket, respectively, and are eventually rearranged in Figure 11. The mean correlation components of quantities denoted by blue paths are sensitive to the choice of the background stratification as argued in section C1.

−2.56 GW with the sign referring to the PEA budget). The energy cycle is terminated by two major sinks. The first sink is the baroclinic HPA flux (2.01 GW) which is due to the radiation of internal gravity waves through the lateral boundaries at $x = \pm 120$ km. The second sink is the dissipation of baroclinic KE by the horizontal viscosity term (0.77 GW).

[23] It is worth noting the significance of nonlinear effects as revealed by two separate quantities. The first nonlinear quantity is the advective conversion between the barotropic and baroclinic KEs (0.49 GW), which originates from the advection term of the horizontal momentum equation (1). The second nonlinear quantity is the flux of PEA (0.45 GW), which originates from the advection term of the density anomaly equation (5).

[24] The above results can be compared with the energy budget of M_2 tides in the Hawaiian Islands region as estimated by *Carter et al.* [2008, hereafter CM08] using a comprehensive three-dimensional hydrostatic model (Table 2). Their experiment has no geostrophic background current, thus could be compared with our experiment without the ITF. The barotropic energy input to the Hawaiian Islands region is 2.733 GW of which 2.286 GW is converted to PEA, and then radiated away by internal gravity waves at a rate of 1.701 GW. These values are comparable to our estimates in the LS region. CM08 comment that the effect of advection is underestimated in their model because little energy is present in other constituents. The baroclinic advection in our model is also small (0.07 GW), however here it is an artifact resulting from the cancelation of the advective conversion (between barotropic and baroclinic KEs, 0.49 GW in Figure 9a) and the PEA flux (−0.45 GW). On the other hand, while it is not clear whether horizontal or vertical mixing is dominant in CM08, the dissipation of baroclinic KE in our model is caused mainly by the horizontal mixing term. Nonhydrostatic models can more accurately resolve signals at higher horizontal wavenumbers (e.g., generation of ISWs and wave breaking over the sill) and hence lead to more horizontal dissipation.

4.2. Case With the ITF (Boreal Summer)

[25] Nonlinear and nonhydrostatic effects are enhanced in this experiment (Figure 9b). The advective conversion

Table 2. Comparisons of the Energy Budgets of Tidal Flows in Lombok Strait and Hawaiian Islands With a Unit of 10^9 W[a]

	Lombok Strait	Hawaiian Islands
Model, resolution	2-D, dx = 140 m	3-D, dx ≃ 1000 m
Water area	0.9×10^{11} m^2	1.2×10^{11} m^2
Type of tide	M2	M2
	Barotropic Energy Budget	
Tendency	0.00	−0.006
∇ · Flux	+3.86	+2.733
Advection	−0.49	+0.005
Conversion	−2.96	−2.286
Dissipation	(−0.26 − 0.13 =) −0.39	−0.163
Nonhydrostatic	−0.01	None
Error	0.00	−0.296
	Baroclinic Energy budget	
Tendency	0.00	+0.054
∇ · Flux	−2.01	−1.701
Advection	(0.49 + 0.03 − 0.45 =) +0.07	−0.016
Conversion	+2.96	+2.340
Dissipation	(−0.17 − 0.77 − 0.03 + 0.02 =) −0.95	−0.445
Nonhydrostatic	+0.01	None
Error	−0.08	−0.125

[a]Energy budgets of tidal flows in Lombok Strait are adapted from Figure 9a of this paper, and those in the Hawaiian Islands are adapted from Table 2 of *Carter et al.* [2008]. The names of the conversion flux terms follow that used by *Carter et al.* [2008], who defined the barotropic energy as the sum of barotropic KE and the PE associated with sea surface height (the latter of which is absent in our formulation), with the baroclinic energy being the sum of baroclinic KE and PEA.

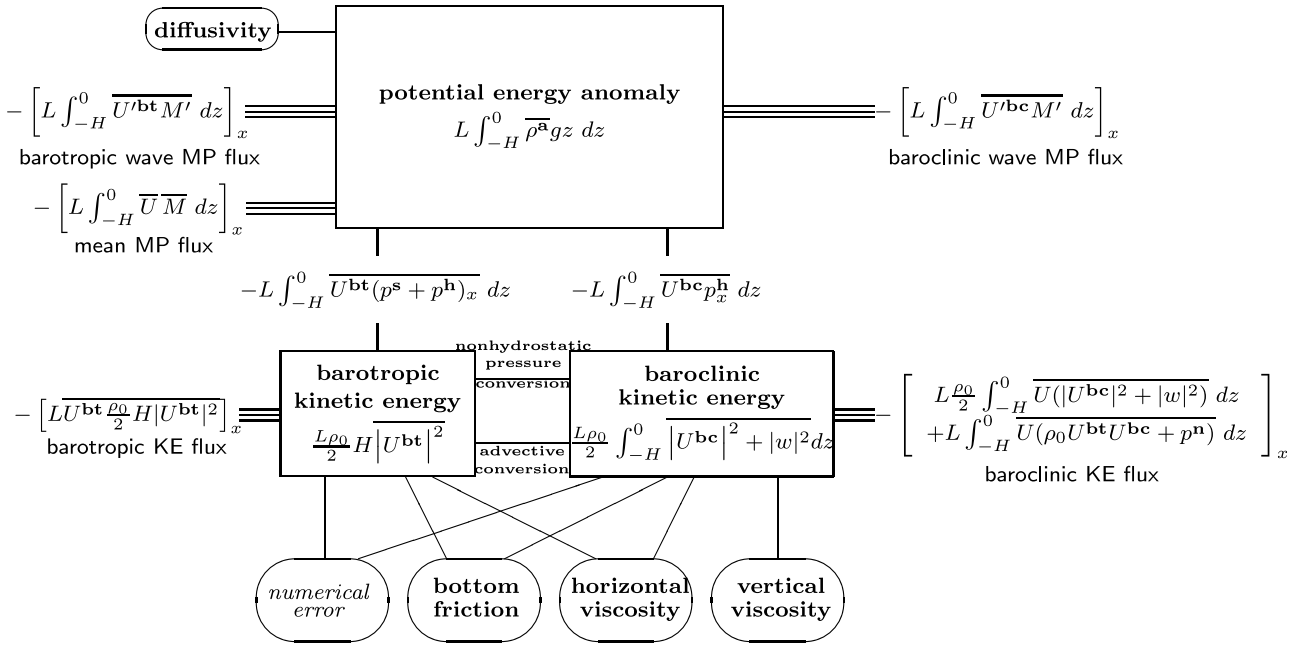

Figure 10. Same as Figure 8 except that it is based on (C7), (C14), and (C17)–(C18). The Montgomery potential (MP) is defined by $M \equiv p^{\mathbf{s}} + p^{\mathbf{h}} + \rho gz$. See section C2.

between barotropic and baroclinic KEs is 0.66 GW with the ITF in comparison to 0.49 GW without it. The nonhydrostatic pressure (NP) conversion between barotropic and baroclinic KEs is 0.12 GW with the ITF (0.01 GW without it). These increased inputs into baroclinic KE are canceled by increases in (1) dissipation by the horizontal and vertical viscosity term (1.29 GW and 0.42 GW with the ITF in contrast to 0.77 GW and 0.17 GW without it, respectively) and (2) the flux of baroclinic KE (0.17 GW with the ITF in contrast to −0.03 GW without it).

[26] We find a decrease in the baroclinic HPA flux (1.28 GW with, in contrast to 2.01 GW without). However, in the presence of time mean flows such as the ITF, it is necessary to distinguish contributions from the mean correlation component and the wave correlation component for each flux/conversion term. Namely $\overline{AB} = \overline{A}\,\overline{B} + \overline{A'B'}$ is considered for arbitrary quantities A and B. For simplicity such a diagnosis has been done for only three separate quantities: the combined barotropic SP and HPA flux, the baroclinic HPA flux, and the PEA flux, as shown by the bracketed values in Figures 9a and 9b. Now the wave correlation component of the baroclinic HPA flux is 1.78 GW with the ITF, and is close to 1.92 GW without it. Likewise the wave correlation component of the PEA flux is 0.69 GW with the ITF, and is close to 0.93 GW without it. In both experiments the wave PEA flux has the same sign as and about half the magnitude of the baroclinic wave HPA flux.

[27] On the other hand the mean correlation component of the baroclinic HPA flux provides an energy input of 0.50 GW with the ITF. The mean correlation component of the PEA flux provides an energy input of 0.48 GW without the ITF. However these values are artificial and not suitable for physical interpretations, because the mean correlation component of quantities involving either the background stratification $\rho^{\mathbf{z}}$ or the associated anomaly $\rho^{\mathbf{a}}$ (i.e., five separate quantities representing the blue paths in each of Figures 9a and 9b) is sensitive to choices of the background stratification. There is no such sensitivity in the wave correlation component, because $\overline{A'\rho^{\mathbf{a}\prime}} = \overline{A'\rho'}$ for an arbitrary quantity A. These sensitivity issues are fundamental aspects of the energy diagnosis of internal waves in the presence of time mean flows (section C1).

[28] In order to avoid the above complexity (i.e., sensitivity to the background stratification) and also to focus on estimating the radiation rate of the overall internal wave fluxes, below we use another energy diagram which is simple and robust in that each conversion/flux term is independent of the definitions of the background stratification and the anomaly (Figure 10 and section C2). The PEA budget is given by the flux divergence of Montgomery potential (MP) defined by $M \equiv p^{\mathbf{s}} + p^{\mathbf{h}} + \rho gz$. The MP has been used in many studies of large-scale or finite amplitude geophysical flows [*Montgomery*, 1938; *Andrews*, 1983; *Pedlosky*, 1996; *Aiki and Richards*, 2008].

[29] The energy input into the barotropic tides is represented by the barotropic wave MP flux whose rate is 4.05 GW with the ITF and slightly less, 3.81 GW, without it (Figure 11). Likewise the energy radiation by finite amplitude and nonlinear internal gravity waves is represented by the baroclinic wave MP flux (i.e., the sum of the baroclinic wave HPA flux and the baroclinic wave PEA flux) at a rate of 2.42 GW with the ITF and a rate of 2.82 GW without it. Although the two experiments give similar rates, the distributions of the baroclinic wave MP flux indicate that the presence of the ITF alters the way that the radiated wave energy is partitioned between the two sides of the sill. Without the ITF (black line in Figure 12d), the baroclinic wave MP flux on the Java Sea side (1.59 GW at $x = 120$ km) is greater in magnitude than that on the Indian Ocean side (−1.23 GW at $x = -120$ km). When the ITF is present (green line), however, the baroclinic wave MP flux on the Java Sea side (0.57 GW at $x = 120$ km) is smaller in magnitude than

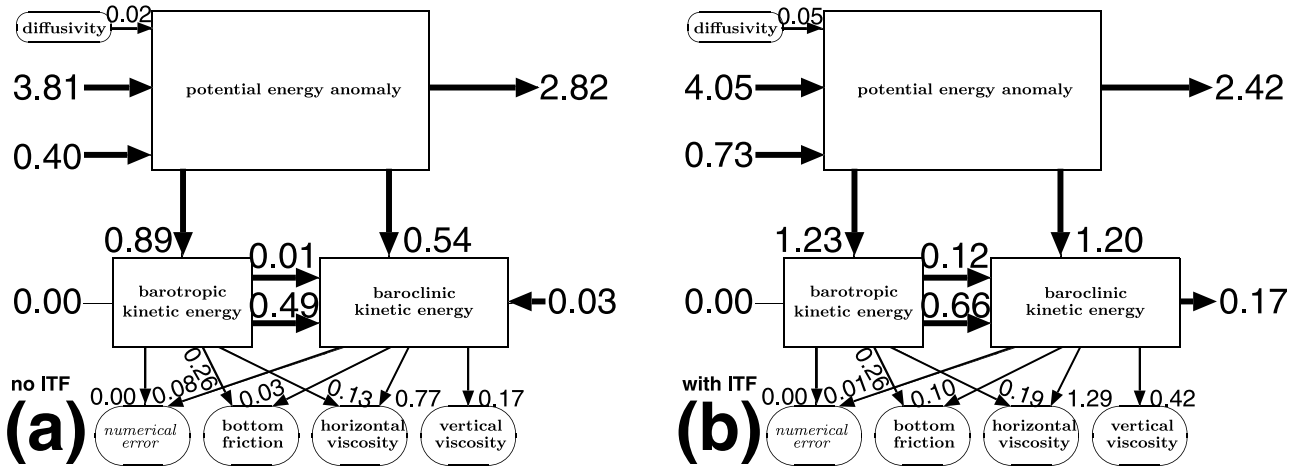

Figure 11. Same as Figure 9 except for being based on the energy diagram of Figure 10.

that on the Indian Ocean side (−1.85 GW at $x = -120$ km). It is interesting that the wave energy flux is less on the Java Sea side despite the fact that there are still more ISWs on this side in Figure 7. This is because the channel is narrower on the Java Sea side (Figure 3), and the energy fluxes are cross-channel integrated values.

[30] These characteristics can be roughly confirmed by the distributions of the baroclinic HPA flux in Figure 12b and are also consistent with the result of Ma11. In the real ocean, waves away from the sill would be eventually dissipated by microscopic mixing. We expect such remote dissipation to be significant on the Java Sea side in the boreal winter and on the Indian Ocean side in the boreal summer. Furthermore, our findings are relevant to the issue of El Niño/La Niña modulation of the ITF and subsequent regulation of the radiated internal wave field, as considered by Ma11.

4.3. Discussion of Time Mean Flows

[31] We explain the energy input by the mean MP flux which is 0.40 GW without the ITF and 0.73 GW with it. The flux can be decomposed into two components

$$\begin{aligned} -L\int_{-H}^{0}\overline{U}\,\overline{M}dz &= -L\int_{-H}^{0}\overline{U}\,\overline{p^{\mathbf{s}}}dz - L\int_{-H}^{0}\overline{U}\left(\overline{p^{\mathbf{h}}}+\overline{\rho}gz\right)dz \\ &= -LH\overline{U}^{\mathbf{bt}}\,\overline{p^{\mathbf{s}}} - \left[L\left(\int_{-H}^{z}\overline{U}d\ddot{z}\right)\left(\overline{p^{\mathbf{h}}}+\overline{\rho}gz\right)\right]\Big|_{z=-H}^{z=0} \\ &\quad + L\int_{-H}^{0}\left(\int_{-H}^{z}\overline{U}d\ddot{z}\right)\left(\overline{p^{\mathbf{h}}}+\overline{\rho}gz\right)_{z}dz \\ &= -LH\overline{U}^{\mathbf{bt}}\,\overline{p^{\mathbf{s}}} + L\int_{-H}^{0}\left(\int_{-H}^{z}\overline{U}d\ddot{z}\right)\overline{\rho}_{z}gzdz, \end{aligned} \tag{7}$$

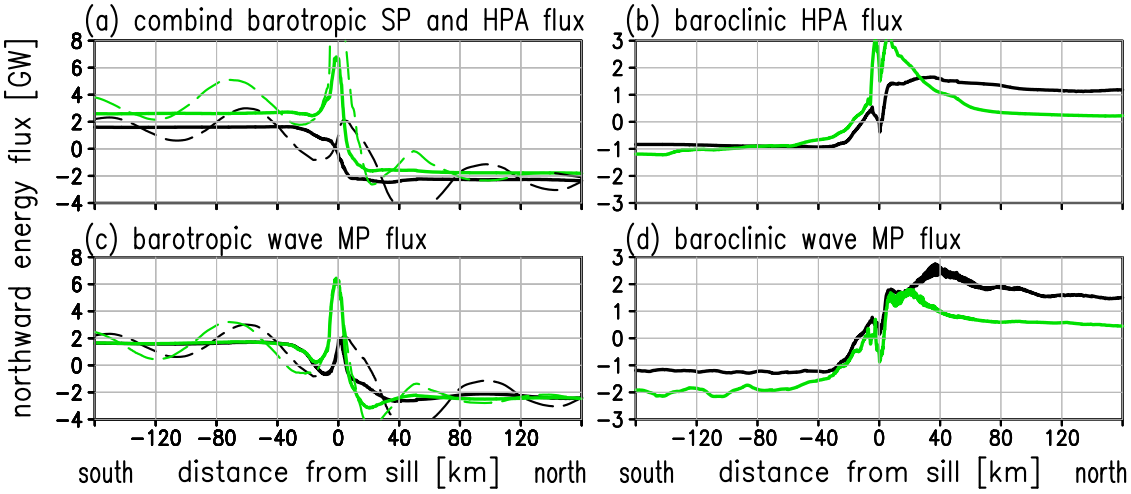

Figure 12. Distributions of various energy fluxes (10^9W, positive northward) in the experiments without the ITF (black) and with it (green): (a) the combined barotropic SP and HPA flux (solid line, $L\int_{-H}^{0}\overline{U^{\mathbf{bt}}(p^{\mathbf{s}}+p^{\mathbf{ha}})}dz$) and the barotropic SP flux (dashed line, $L\int_{-H}^{0}\overline{U^{\mathbf{bt}}p^{\mathbf{s}}}dz$), (b) the baroclinic HPA flux $L\int_{-H}^{0}\overline{U^{\mathbf{bc}}p^{\mathbf{ha}}}dz$, (c) the barotropic wave MP flux (solid line, $L\int_{-H}^{0}\overline{U'^{\mathbf{bt}}M'}dz$) and the barotropic wave SP flux (dashed line, $L\int_{-H}^{0}\overline{U'^{\mathbf{bt}}p^{\mathbf{s}\prime}}dz$), and (d) the baroclinic wave MP flux $L\int_{-H}^{0}\overline{U'^{\mathbf{bc}}M'}dz$, all of which are time averaged for the last five M_2 cycles of the integration period.

where $\overline{U}$ is a function of $\ddot{z}$ in calculating $\int_{-H}^{z} \overline{U} d\ddot{z}$ and integration by parts has been used with a boundary condition of $p^{\mathbf{h}} + \rho g z = 0$ at the sea surface at $z = 0$. The first term on the right hand side is the product of the depth-integrated transport $H\overline{U}^{\mathbf{bt}}$ and the sea surface pressure. The second term is the depth integral of the product of three separate quantities: the time mean transport from the bottom to a given depth $\int_{-H}^{z} \overline{U} d\ddot{z}$, the vertical gradient of the time mean density $\overline{\rho}_z$, and the depth z. (The physical meaning of this term might be inferred from the case of the classical two-layer hydraulic control where the difference of the depths of the layer interface upstream and downstream of the sill is most important.)

[32] There are no barotropic time mean flows in the experiment without the ITF, resulting in the first term on the right hand side of (7) being zero. All of the energy input of 0.40 GW comes from the second term on the right hand side of (7), which is associated with time mean baroclinic overturning circulations of ±0.5 Sv in amplitude that are established after the propagation of long waves in the second and higher vertical modes (not shown). These long waves appear to originate from hydraulic-jump-like overturning [cf. *Legg and Klymak*, 2008] whose signals can be found at around (x,z) = (15 km, −150 m) and (−10 km, −200 m) in Figure 5, and propagate into both sides of the sill. The generation mechanism of these long waves and the time mean overturning circulations needs further investigation. *Buijsman et al.* [2010] report the presence of similar time mean overturning circulations associated with tidally generated ISWs in the South China Sea.

[33] On the other hand the first term on the right hand side of (7) is 1.30 GW in the experiment with the ITF where $L H \overline{U}^{\mathbf{bt}} = -5.2$ Sv in all regions. This indicates that the time mean SP is higher on the Java Sea side and lower on the Indian Ocean side. We have confirmed that the time mean sea surface height has a difference of about 2.5 cm between $x = -120$ km and $x = 120$ km in this experiment. The model ITF is accelerated by this net northward gradient in the sea surface height. Simultaneously the model ITF is decelerated by interaction with high-amplitude waves over the sill (which might suggest the presence of internal wave form drag). This balance maintains the strength of the model ITF.

5. Summary

[34] Lombok Strait is one of the major passages supporting the Indonesian Throughflow (ITF), and is known to have a sharply defined sill resulting in strong tidal flows. One of the aims of this study is to examine the observed seasonality of internal solitary-like waves obtained by Ma11 in the light of results derived from our numerical study. In order to investigate the possible impact of the ITF on tidally generated internal gravity waves in LS and their energetics, we use a nonhydrostatic numerical model which is forced by barotropic volume fluxes oscillating at the M_2 tidal period. The model solves for fluid motion in the vertical plane aligned along the main axis of the strait, and takes into account the variable width of the strait region with assuming radial propagation of waves away from the sill.

[35] Two main experiments have been performed, one without and one with an idealized ITF component flowing southward in the upper layer. These experiments correspond to conditions in boreal winter and summer (or in El Niño and La Niña years), respectively. Both experiments show trains of internal solitary-like gravity waves with a large number of waves formed in the northward propagating wave trains, that we attribute to the narrower channel width on that side. In both experiments about 3.9 GW of energy is injected into the barotropic tides, of which about 2.6 GW is radiated away by internal gravity waves. (These approximated values are based on (3.81 + 4.05)/2 = 3.930 GW and (2.82 + 2.42)/2 = 2.620 GW from Figure 11.) Although similar values are obtained in both experiments, the ITF regulates the partition of radiated energy between the two sides of the sill. The net energy radiation is northward without the ITF and southward with it. Such a view is obtained by diagnosing the flux of the Montgomery potential which takes into account the effect of finite amplitude waves. Waves away from the sill would be eventually dissipated by microscopic mixing either near shores or in deep oceans, which should be confirmed by future field measurements of turbulent kinetic energy and wave breaking in the LS region.

[36] Future numerical studies using a three-dimensional nonhydrostatic model will be able to take into account the effects of (1) the rotation of the earth, (2) lateral variations in the background density field in geostrophic balance with a spatially varying ITF, (3) the seasonal change in the stratification in the LS region, and (4) the phase difference of barotropic tides on the Indian Ocean and Java Sea sides of the sill. Even when such realistic modeling is attempted, the energy diagnosis based on the Montgomery potential can still be easily used without any practical modifications, because it does not require the background stratification density to be defined.

Appendix A: Derivation of Model Equations

[37] We consider Cartesian coordinates (x, y, z) with the x and y axes parallel to the main and subaxes of the strait, respectively (Figure 3). The velocity component in the direction of each axis of (x, y, z) is represented by (u, v, w). The Boussinesq nonhydrostatic incompressible equations governing the fluid motion are

$$\rho_0 \left[u_t + u u_x + v u_y + w u_z \right] = -p_x, \tag{A1}$$

$$\rho_0 \left[v_t + u v_x + v v_y + w v_z \right] = -p_y, \tag{A2}$$

$$\rho_0 \left[w_t + u w_x + v w_y + w w_z \right] = -p_z^{\mathbf{n}}, \tag{A3}$$

$$0 = -p_z^{\mathbf{h}} - \rho g, \tag{A4}$$

$$u_x + v_y + w_z = 0, \tag{A5}$$

$$\rho_t + u \rho_x + v \rho_y + w \rho_z = 0. \tag{A6}$$

The rotation of the Earth is not considered because width-averaged equations cannot describe coastal Kelvin waves.

A1. Curvilinear Orthogonal Coordinates

[38] We consider generalized curvilinear coordinates (ξ, η, z) with ξ and η being analogous to the radius and angle in polar coordinates (Figure 3). ξ increases (decreases) as one moves in the direction of the Java Sea (Indian Ocean) side. η increases (decreases) as one moves in the direction of the Bali (Lombok) island coast. The three-dimensional vector (U, V, w) represents the velocity in the (ξ, η, z) directions.

$$\rho_0\left[U_t+\frac{1}{h^\xi}UU_\xi+\frac{1}{h^\eta}VU_\eta+wU_z+\frac{1}{h^\xi h^\eta}V\left(Uh^\xi_\eta-Vh^\eta_\xi\right)\right]=-\frac{1}{h^\xi}p_\xi, \tag{A7}$$

$$\rho_0\left[V_t+\frac{1}{h^\xi}UV_\xi+\frac{1}{h^\eta}VV_\eta+wV_z+\frac{1}{h^\xi h^\eta}U\left(Vh^\eta_\xi-Uh^\xi_\eta\right)\right]=-\frac{1}{h^\eta}p_\eta, \tag{A8}$$

$$\rho_0\left[w_t+\frac{1}{h^\xi}Uw_\xi+\frac{1}{h^\eta}Vw_\eta+ww_z\right]=-p^{\mathbf{n}}_z, \tag{A9}$$

$$0=-p^{\mathbf{h}}_z-\rho g, \tag{A10}$$

$$\frac{1}{h^\xi h^\eta}\left[(h^\eta U)_\xi+\left(h^\xi V\right)_\eta\right]+w_z=0, \tag{A11}$$

$$\rho_t+\frac{1}{h^\xi}U\rho_\xi+\frac{1}{h^\eta}V\rho_\eta+w\rho_z=0, \tag{A12}$$

where $h^\xi[\xi,\eta]$ and $h^\eta[\xi,\eta]$ are positive scale factors in the (ξ, η) coordinates [*Batchelor*, 1967]. The above equations can be rewritten using flux divergences

$$\rho_0\left[\left(h^\xi h^\eta U\right)_t+(h^\eta UU)_\xi+\left(h^\xi VU\right)_\eta+\left(h^\xi h^\eta wU\right)_z+V\left(Uh^\xi_\eta-Vh^\eta_\xi\right)\right]=-h^\eta p_\xi, \tag{A13}$$

$$\rho_0\left[\left(h^\xi h^\eta V\right)_t+(h^\eta UV)_\xi+\left(h^\xi VV\right)_\eta+\left(h^\xi h^\eta wV\right)_z+U\left(Vh^\eta_\xi-Uh^\xi_\eta\right)\right]=-h^\xi p_\eta, \tag{A14}$$

$$\rho_0\left[\left(h^\xi h^\eta w\right)_t+(h^\eta Uw)_\xi+\left(h^\xi Vw\right)_\eta+\left(h^\xi h^\eta ww\right)_z\right]=-h^\xi h^\eta p^{\mathbf{n}}_z, \tag{A15}$$

$$0=-p^{\mathbf{h}}_z-\rho g, \tag{A16}$$

$$(h^\eta U)_\xi+\left(h^\xi V\right)_\eta+\left(h^\xi h^\eta w\right)_z=0, \tag{A17}$$

$$h^\xi h^\eta\rho_t+(h^\eta U\rho)_\xi+\left(h^\xi V\rho\right)_\eta+\left(h^\xi h^\eta w\rho\right)_z=0. \tag{A18}$$

A2. Width Averaging and the Leading Order Equations

[39] One way to measure the width of the strait region is to follow each line of constant ξ

$$L[\xi]=\int_{\eta^l}^{\eta^b}h^\eta d\eta, \tag{A19}$$

where η^b and η^l indicate the coastlines of the Bali and Lombok islands, respectively. The width average of an arbitrary quantity $A[\xi,\eta,z,t]$ can be defined as

$$\widetilde{A}[\xi,z,t]=\frac{\int_{\eta^l}^{\eta^b}h^\eta A d\eta}{L}. \tag{A20}$$

This enables us to consider separation of A into mean and deviation components

$$A[\xi,\eta,z,t]=\widetilde{A}[\xi,z,t]+A''[\xi,\eta,z,t]. \tag{A21}$$

Below this separation is applied to all quantities (except for $h^\xi[\xi,\eta]=\widetilde{h}^\xi[\xi]+h^{\xi\prime\prime}[\xi,\eta]$). We now assume $A''\ll\widetilde{A}$ for each of U, V, w, $p^{\mathbf{s}}$, $p^{\mathbf{h}}$, $p^{\mathbf{n}}$, ρ, and h^ξ (which includes the approximation of radial propagation of waves away from the sill) and substitute them to (A13)–(A18). The leading order equations become

$$\rho_0\left[\left(\widetilde{h}^\xi h^\eta\widetilde{U}\right)_t+\left(h^\eta\widetilde{U}\widetilde{U}\right)_\xi+\left(\widetilde{h}^\xi h^\eta\widetilde{w}\widetilde{U}\right)_z-\widetilde{V}\widetilde{V}h^\eta_\xi\right]=-h^\eta\widetilde{p}_\xi, \tag{A22}$$

$$\rho_0\left[\left(\widetilde{h}^\xi h^\eta\widetilde{V}\right)_t+\left(h^\eta\widetilde{U}\widetilde{V}\right)_\xi+\left(\widetilde{h}^\xi h^\eta\widetilde{w}\widetilde{V}\right)_z+\widetilde{U}\widetilde{V}h^\eta_\xi\right]=0, \tag{A23}$$

$$\rho_0\left[\left(\widetilde{h}^\xi h^\eta\widetilde{w}\right)_t+\left(h^\eta\widetilde{U}\widetilde{w}\right)_\xi+\left(\widetilde{h}^\xi h^\eta\widetilde{w}\widetilde{w}\right)_z\right]=-\widetilde{h}^\xi h^\eta\widetilde{p}^{\mathbf{n}}_z, \tag{A24}$$

$$0=-\widetilde{p}^{\mathbf{h}}_z-\widetilde{\rho}g, \tag{A25}$$

$$\left(h^\eta\widetilde{U}\right)_\xi+\left(\widetilde{h}^\xi h^\eta\widetilde{w}\right)_z=0, \tag{A26}$$

$$\widetilde{h}^\xi h^\eta\widetilde{\rho}_t+\left(h^\eta\widetilde{U}\widetilde{\rho}\right)_\xi+\left(\widetilde{h}^\xi h^\eta\widetilde{w}\widetilde{\rho}\right)_z=0. \tag{A27}$$

The width integral of (A22)–(A27) yields

$$\rho_0\left[\left(\widetilde{h}^\xi L\widetilde{U}\right)_t+\left(L\widetilde{U}\widetilde{U}\right)_\xi+\left(\widetilde{h}^\xi L\widetilde{w}\widetilde{U}\right)_z-\widetilde{V}\widetilde{V}L_\xi\right]=-L\widetilde{p}_\xi, \tag{A28}$$

$$\rho_0\left[\left(\widetilde{h}^\xi L\widetilde{V}\right)_t+\left(L\widetilde{U}\widetilde{V}\right)_\xi+\left(\widetilde{h}^\xi L\widetilde{w}\widetilde{V}\right)_z+\widetilde{U}\widetilde{V}L_\xi\right]=0, \tag{A29}$$

$$\rho_0\left[\left(\widetilde{h}^\xi L\widetilde{w}\right)_t+\left(L\widetilde{U}\widetilde{w}\right)_\xi+\left(\widetilde{h}^\xi L\widetilde{w}\widetilde{w}\right)_z\right]=-\widetilde{h}^\xi L\widetilde{p}^{\mathbf{n}}_z, \tag{A30}$$

$$0=-\widetilde{p}^{\mathbf{h}}_z-\widetilde{\rho}g, \tag{A31}$$

$$\left(L\widetilde{U}\right)_{\xi}+\left(\widetilde{h}^{\xi}L\widetilde{w}\right)_{z}=0, \tag{A32}$$

$$\widetilde{h}^{\xi}L\widetilde{\rho}_{t}+\left(L\widetilde{U}\widetilde{\rho}\right)_{\xi}+\left(\widetilde{h}^{\xi}L\widetilde{w}\widetilde{\rho}\right)_{z}=0. \tag{A33}$$

A3. Mapping From (ξ, z, t) Coordinates to (x, z, t) Coordinates

[40] We consider each line of fixed η. Each line should cross the sill, at a position denoted by $\xi = \xi^{s}[\eta]$. The distance between the sill and a point (ξ, η) is measured by $\int_{\xi^{s}}^{\xi} h^{\xi}\, d\xi$. Although referred to as a distance, this quantity is signed in such a way as to become positive on the Java Sea side and negative on the Indian Ocean side. The width average of the distance gives a reference for mapping from (ξ, z, t) coordinates to (x, z, t) coordinates [cf. *Jacobson and Aiki*, 2006]. This is achieved by replacing $\frac{\partial}{\widetilde{h}^{\xi}\partial\xi}$ in (A28)–(A33) with $\frac{\partial}{\partial x}$

$$\rho_{0}\left[\left(L\widetilde{U}\right)_{t}+\left(L\widetilde{U}\widetilde{U}\right)_{x}+\left(L\widetilde{w}\widetilde{U}\right)_{z}-\widetilde{V}\widetilde{V}L_{x}\right]=-L\widetilde{p}_{x}, \tag{A34}$$

$$\rho_{0}\left[\left(L\widetilde{V}\right)_{t}+\left(L\widetilde{U}\widetilde{V}\right)_{x}+\left(L\widetilde{w}\widetilde{V}\right)_{z}+\widetilde{U}\widetilde{V}L_{x}\right]=0, \tag{A35}$$

$$\rho_{0}\left[(L\widetilde{w})_{t}+\left(L\widetilde{U}\widetilde{w}\right)_{x}+(L\widetilde{w}\widetilde{w})_{z}\right]=-L\widetilde{p}_{z}^{\mathbf{n}}, \tag{A36}$$

$$0=-\widetilde{p}_{z}^{\mathbf{h}}-\widetilde{\rho}g, \tag{A37}$$

$$\left(L\widetilde{U}\right)_{x}+(L\widetilde{w})_{z}=0, \tag{A38}$$

$$L\widetilde{\rho}_{t}+\left(L\widetilde{U}\widetilde{\rho}\right)_{x}+(L\widetilde{w}\widetilde{\rho})_{z}=0. \tag{A39}$$

A no-normal-flow boundary condition at the coastlines of the Bali and Lombok islands is $V = 0$ at $\eta = \eta^{b}$ and $\eta = \eta^{l}$, respectively. Examination of (A34)–(A39) suggests that the set of equations is self consistent even if $V = 0$, in such case (A34)–(A39) become

$$\rho_{0}\left[\left(L\widetilde{U}\right)_{t}+\left(L\widetilde{U}\widetilde{U}\right)_{x}+\left(L\widetilde{w}\widetilde{U}\right)_{z}\right]=-L\widetilde{p}_{x}, \tag{A40}$$

$$\rho_{0}\left[(L\widetilde{w})_{t}+\left(L\widetilde{U}\widetilde{w}\right)_{x}+(L\widetilde{w}\widetilde{w})_{z}\right]=-L\widetilde{p}_{z}^{\mathbf{n}}, \tag{A41}$$

$$0=-\widetilde{p}_{z}^{\mathbf{h}}-\widetilde{\rho}g, \tag{A42}$$

$$\left(L\widetilde{U}\right)_{x}+(L\widetilde{w})_{z}=0, \tag{A43}$$

$$L\widetilde{\rho}_{t}+\left(L\widetilde{U}\widetilde{\rho}\right)_{x}+(L\widetilde{w}\widetilde{\rho})_{z}=0. \tag{A44}$$

(A40)–(A44) are expressed with flux divergences, which can be rewritten into (1)–(4) where the Lagrangian derivative is used and the tilde symbol is dropped for simplicity.

Appendix B: Sea Surface Pressure

[41] The model actually solves a linearized free sea surface equation: $L[p^{\mathbf{s}}/(\rho_{0}g)]_{t}+(L\int_{-H}^{0} Udz)_{x}=0$ where $p^{\mathbf{s}}/(\rho_{0}g)$ is the sea surface height and H is the time-independent total depth. This equation is solved by an implicit method, called the semi-implicit scheme of *Dukowicz and Smith* [1994]. Application of a time average yields $(L\int_{-H}^{0} Udz)_{x}=0$ which indicates that the time average of w at $z = 0$ is zero, whereas the perturbation of w is nonzero at $z = 0$. Our choice of the free sea surface scheme is based on a preliminary result that the rigid sea surface scheme produces numerical noise associated with the stepped bottom slope in the z coordinate model. The noise is invisible in the fields of velocity and density, but disturbs the diagnosis of the energy fluxes and budgets.

[42] To summarize, the semi-implicit free sea surface scheme achieves more realistic physics with less computational cost compared with the rigid sea surface scheme. The use of the rigid sea surface formulation for diagnosing the output of a free sea surface model would yield an inconsistency in the energy budget if the sea surface displacement was too large. We have computed the size of the associated errors, which turned out to be less than 0.01 GW (if computed in the same manner as for the other physical terms in section 4) and is negligible. Note that our energy diagnosis has (1) time mean flows, (2) nonhydrostatic effects, (3) an improved equation for potential energy anomaly, and (4) implicit consideration of where to locate the pressure-flux divergence equation. Neither *Niwa and Hibiya* [2004] nor *Carter et al.* [2008] took these aspects into account. The use of the rigid formulation helps readers to focus on the issues addressed in the present study.

Appendix C: Energy Equations

[43] Using (1)–(3) and (5) one can derive equations for the horizontal and vertical components of KE, the divergence of the SP, HPA, NP fluxes, and the PEA

$$\left(L\frac{\rho_{0}}{2}|U|^{2}\right)_{t}+\left(LU\frac{\rho_{0}}{2}|U|^{2}\right)_{x}+\left(Lw\frac{\rho_{0}}{2}|U|^{2}\right)_{z}=-LUp_{x}+LUD^{U}, \tag{C1}$$

$$\left(L\frac{\rho_{0}}{2}|w|^{2}\right)_{t}+\left(LU\frac{\rho_{0}}{2}|w|^{2}\right)_{x}+\left(Lw\frac{\rho_{0}}{2}|w|^{2}\right)_{z}=-Lwp_{z}^{\mathbf{n}}+LwD^{w}, \tag{C2}$$

$$(LUp^{\mathbf{s}})_{x}+(Lwp^{\mathbf{s}})_{z}=LUp_{x}^{\mathbf{s}}, \tag{C3}$$

$$\left(LUp^{\mathbf{ha}}\right)_{x}+\left(Lwp^{\mathbf{ha}}\right)_{z}=LUp_{x}^{\mathbf{ha}}+Lwp_{z}^{\mathbf{ha}}=LUp_{x}^{\mathbf{h}}-L\rho^{\mathbf{a}}gw, \tag{C4}$$

$$(LUp^{\mathbf{n}})_{x}+(Lwp^{\mathbf{n}})_{z}=LUp_{x}^{\mathbf{n}}+Lwp_{z}^{\mathbf{n}}, \tag{C5}$$

$$(L\rho^{\mathbf{a}}gz)_t+\left[LU\left(\rho gz+p^{\mathbf{hz}}\right)\right]_x+\left[Lw\left(\rho gz+p^{\mathbf{hz}}\right)\right]_z = L\rho^{\mathbf{a}}gw+LgzD^{\rho}, \quad \text{(C6)}$$

where $p_x^{\mathbf{ha}}=p_x^{\mathbf{h}}$ and $p_z^{\mathbf{ha}}=-\rho^{\mathbf{a}}gz$ have been used on the right hand side of (C4). The PEA equation (C6) is exact but has not been shown before the present study.

[44] Below (U, w) is decomposed into barotropic velocity $(U^{\mathbf{bt}}, w^{\mathbf{bt}})$ and baroclinic velocity $(U^{\mathbf{bc}}, w^{\mathbf{bc}})$, each of which satisfies the incompressibility condition (3) and a no-normal-flow condition at the top and bottom of the ocean. Noting that $\int_{-H}^{0}|U^{\mathbf{bt}}+U^{\mathbf{bc}}|^2dz=\int_{-H}^{0}|U^{\mathbf{bt}}|^2+|U^{\mathbf{bc}}|^2dz$, the depth integral of the horizontal KE equation (C1) can be separated into

$$\underbrace{\left(LH\frac{\rho_0}{2}\left|U^{\mathbf{bt}}\right|^2\right)_t}_{\text{barotropic KE}}+\underbrace{\left(LU^{\mathbf{bt}}H\frac{\rho_0}{2}\left|U^{\mathbf{bt}}\right|^2\right)_x}_{\text{barotropic KE flux}} = \underbrace{Adv}_{\text{Advconv}}+L\int_{-H}^{0}[-\underbrace{U^{\mathbf{bt}}\left(p_x^{\mathbf{s}}+p_x^{\mathbf{h}}\right)}_{\text{SHPconv(bt)}}-\underbrace{U^{\mathbf{bt}}p_x^{\mathbf{n}}}_{\text{NPconv}}+U^{\mathbf{bt}}D^U]dz, \quad \text{(C7)}$$

$$\left(L\int_{-H}^{0}\frac{\rho_0}{2}|U^{\mathbf{bc}}|^2dz\right)_t+\left[L\int_{-H}^{0}U\left(\frac{\rho_0}{2}|U^{\mathbf{bc}}|^2+\rho_0U^{\mathbf{bt}}U^{\mathbf{bc}}\right)dz\right]_x = -Adv+L\int_{-H}^{0}U^{\mathbf{bc}}\left(-p_x^{\mathbf{h}}-p_x^{\mathbf{n}}+D^U\right)dz, \quad \text{(C8)}$$

where $Adv\equiv-\rho_0U^{\mathbf{bt}}(L\int_{-H}^{0}U^{\mathbf{bc}}U^{\mathbf{bc}}dz)_x$. The Advconv and NPconv terms of (C7) represent the advective (nonlinear) and nonhydrostatic pressure (NP) conversions, respectively, between barotropic and baroclinic KEs. The depth integral of the sum of (C2) and (C5) becomes

$$\left(L\int_{-H}^{0}\frac{\rho_0}{2}|w|^2dz\right)_t+\left[L\int_{-H}^{0}U\left(\frac{\rho_0}{2}|w|^2+p^{\mathbf{n}}\right)dz\right]_x = L\int_{-H}^{0}Up_x^{\mathbf{n}}+wD^wdz. \quad \text{(C9)}$$

The depth integral of (C3) becomes

$$\left(LU^{\mathbf{bt}}Hp^{\mathbf{s}}\right)_x=LU^{\mathbf{bt}}Hp_x^{\mathbf{s}}, \quad \text{(C10)}$$

which is derived using $(LU^{\mathbf{bt}})_x+(Lw^{\mathbf{bt}})_z=0$. The depth integral of (C4) can be separated into

$$\left(LU^{\mathbf{bt}}\int_{-H}^{0}p^{\mathbf{ha}}dz\right)_x=LU^{\mathbf{bt}}\int_{-H}^{0}p_x^{\mathbf{h}}dz-L\int_{-H}^{0}\rho^{\mathbf{a}}gw^{\mathbf{bt}}dz, \quad \text{(C11)}$$

$$\underbrace{\left(L\int_{-H}^{0}U^{\mathbf{bc}}p^{\mathbf{ha}}dz\right)_x}_{\text{baroclinic HPA flux}}=L\int_{-H}^{0}\underbrace{U^{\mathbf{bc}}p_x^{\mathbf{h}}}_{\text{HPconv(bc)}}dz-L\int_{-H}^{0}\underbrace{\rho^{\mathbf{a}}gw^{\mathbf{bc}}}_{\text{Buoconv(bc)}}dz, \quad \text{(C12)}$$

the latter of which is derived by using $(LU^{\mathbf{bc}})_x+(Lw^{\mathbf{bc}})_z=0$.

[45] Finally the depth integral of (C6) is written as

$$\underbrace{\left(L\int_{-H}^{0}\rho^{\mathbf{a}}gzdz\right)_t}_{\text{PEA}}+\underbrace{\left[L\int_{-H}^{0}U\left(\rho gz+p^{\mathbf{hz}}\right)dz\right]_x}_{\text{PEA flux}} = L\int_{-H}^{0}\Big(\underbrace{\rho^{\mathbf{a}}gw^{\mathbf{bt}}}_{\text{Buoconv(bt)}}+\underbrace{\rho^{\mathbf{a}}gw^{\mathbf{bc}}}_{\text{Buoconv(bc)}}\Big)dz+L\int_{-H}^{0}gzD^{\rho}dz, \quad \text{(C13)}$$

where the Buoconv(bt) and Buoconv(bc) terms represent buoyancy conversions associated with the barotropic and baroclinic components of velocity, respectively. The Buoconv(bt) term is also called the topographic conversion because $w^{\mathbf{bt}}\equiv U^{\mathbf{bt}}H_xz/H=0$ if $H_x=0$.

[46] Equations (C7)–(C13) can be used to complete the energy diagram in Figure 8, where (C8) and (C9) are combined to represent the single box of baroclinic KE for simplicity. Namely,

$$\underbrace{\left[L\int_{-H}^{0}\frac{\rho_0}{2}\left(|U^{\mathbf{bc}}|^2+|w|^2\right)dz\right]_t}_{\text{baroclinic KE}}+\underbrace{\left[L\int_{-H}^{0}U\left(\frac{\rho_0}{2}|U^{\mathbf{bc}}|^2+\rho_0U^{\mathbf{bt}}U^{\mathbf{bc}}+\frac{\rho_0}{2}|w|^2+p^{\mathbf{n}}\right)dz\right]_x}_{\text{baroclinic KE flux}} = -\underbrace{Adv}_{\text{Advconv}}+L\int_{-H}^{0}\Big(-\underbrace{U^{\mathbf{bc}}p_x^{\mathbf{h}}}_{\text{HPconv(bc)}}+\underbrace{U^{\mathbf{bt}}p_x^{\mathbf{n}}}_{\text{NPconv}}+U^{\mathbf{bc}}D^U+wD^w\Big)dz, \quad \text{(C14)}$$

where the Advconv and NPconv terms are linked to the barotropic KE equation (C7). The HPconv(bc) term is linked to the baroclinic HPA flux equation (C12).

[47] On the other hand, it is necessary to merge (C10) with (C11)

$$\underbrace{\left[LU^{\mathbf{bt}}\int_{-H}^{0}\left(p^{\mathbf{s}}+p^{\mathbf{ha}}\right)dz\right]_x}_{\text{combined barotropic SP and HPA flux}} = L\int_{-H}^{0}\underbrace{U^{\mathbf{bt}}\left(p^{\mathbf{s}}+p^{\mathbf{h}}\right)_x}_{\text{SHPconv(bt)}}dz-L\int_{-H}^{0}\underbrace{\rho^{\mathbf{a}}gw^{\mathbf{bt}}}_{\text{Buoconv(bt)}}dz, \quad \text{(C15)}$$

where the divergence of the combined barotropic SP and HPA flux on the left hand side represents the barotropic energy input. The combination of SP and HPA is necessary for this energy input to be determined robustly. See Figure 12a where the combined barotropic SP and HPA flux (solid lines) is uniformly distributed in regions away from the sill. This is in contrast to each of the SP flux and the barotropic HPA flux having stationary signals offsetting each other (the former of which is plotted by dashed lines in Figure 12a). The SHPconv (bt) term of (C15) is linked to the barotropic KE equation (C7), and the Buoconv(bt) term is linked to the PEA equation (C13).

C1. Previous Diagram

[48] The prototype of the energy diagram, for diagnosing the topographic conversion of barotropic tides to baroclinic tides and the energy radiation by internal gravity waves,

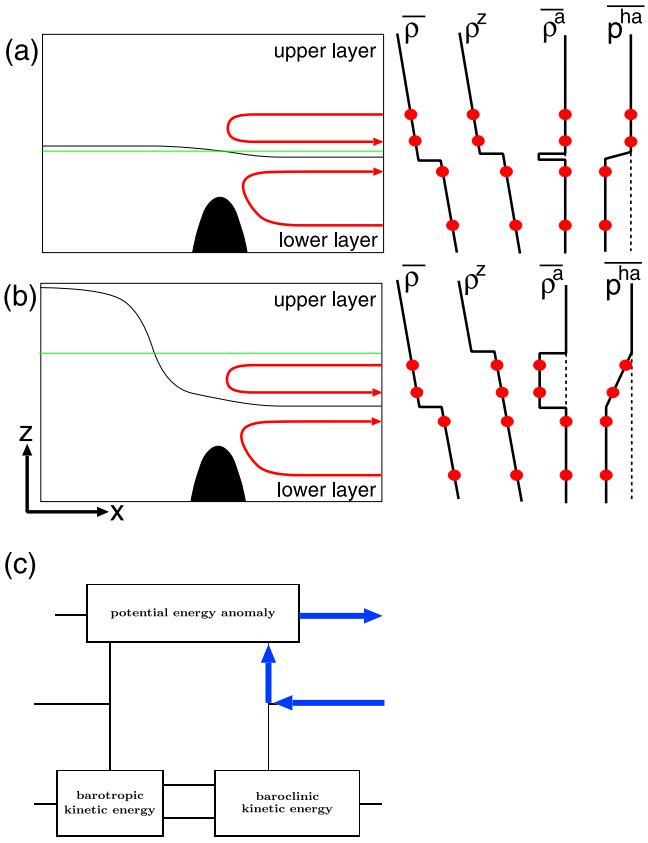

Figure C1. (a and b) The side views of a two-layer ocean with each layer being weakly and uniformly stratified. The black line is the time mean layer interface with the green line being the height of the interface for background stratification. The red arrow is a time mean overturning circulation which is connected to an open boundary at the right edge of the illustrated domain. For Figures C1a and C1b, the vertical profiles of $\overline{\rho}$, $\rho^{\mathbf{z}}$, $\overline{\rho}^{\mathbf{a}}$, and $p^{\mathbf{ha}}$ at the open boundary are illustrated (positive to the right). The red circles on the vertical profiles indicate the depths of the incoming and outgoing flows associated with the time mean overturning circulation. While there is no HPA flux in the case of Figure C1a, there is an incoming HPA flux in the case of Figure C1b resulting in (c) an energy cycle as illustrated using the diagram of Figure 8.

is given by *Niwa and Hibiya* [2004, hereafter NH04] and CM08 who considered the budgets of 'barotropic and baroclinic energies'. The barotropic energy is defined by (the sum of) barotropic KE (and the potential energy of sea surface height, which is absent in our formulation), whose equation is given by merging (C7) and (C15) resulting in the budget of the barotropic energy illustrated by the pink-shaded box in Figure 8. The baroclinic energy is defined by the sum of baroclinic KE and the internal PEA, whose equation is given by merging (C12), (C13), and (C14) with the associated budget illustrated by paths connecting to the green-shaded box in Figure 8. While NH04 and CM08 used an approximated equation for the available potential energy, we use the exact equation (C13) for the PEA.

[49] Although the local value of the PEA flux varies if the reference of the vertical coordinate is changed (which is fixed at the sea surface in the present study), the net PEA flux into an open domain is independent of the reference of the vertical coordinate. In order to show this we consider an open domain whose lateral boundaries are located at $x = x_a$ and $x = x_b$. The volume integral of the divergence of the PEA flux is

$$\left[L\int_{-H}^{0} U\left(\rho g z + p^{\mathbf{hz}}\right)dz\right]_{x=x_a}^{x=x_b} = \left[L\int_{-H}^{0} U\left(\rho g (z-z_0) + p^{\mathbf{hz}}\right)dz\right]_{x=x_a}^{x=x_b}, \tag{C16}$$

where the left hand side assumes that the reference of the vertical coordinate is at the sea surface and the right hand side assumes that it is at $z = z_0$. The above identity holds as far as there is no net mass flux into the domain: $[L\int_{-H}^{0} U\rho dz]_{x=x_a}^{x=x_b} = 0$. Because we eventually consider the energy budget of a statistically equilibriated state, the conservation of mass is always satisfied and we do not have to worry about the sensitivity on the reference of the vertical coordinate.

[50] To summarize the advantages and disadvantages of this diagram, the advantages are as follows: (1) The divergence of the barotropic SP flux on the left hand side of (C10), which is the source of the energy cycle, is partially connected to the budget of the barotropic KE, which is suitable for explaining sequentially how barotropic tidal flows are converted to baroclinic tidal flows or waves. (2) Conversions between the barotropic and baroclinic energies are represented by the following three distinct terms: first the topographic conversion $g\rho^{\mathbf{a}}w^{\mathbf{bt}}$, second the advective conversion of KE, and third the NP conversion, the last two of which are not addressed in NH04 and CM08. (3) The radiation of linear waves is represented by the baroclinic HPA flux [cf. *Cummins and Oey*, 1997; *Nash and Alford*, 2005] and the advection of PEA (i.e., a nonlinear effect) is represented by the PEA flux; the diagram is suitable for the purpose of comparing the linear and nonlinear effects.

[51] The disadvantages are as follows: (1) In the presence of a time mean flow, energy flux/conversion terms need to be decomposed into the mean correlation and the wave correlation (e.g., $\overline{AB} = \overline{A}\,\overline{B} + \overline{A'B'}$ for arbitrary quantities A and B with the overbar and prime symbols representing the Eulerian time mean and deviation, respectively); this would introduce many more paths into the diagram, making it more complicated. (2) In such case, the mean correlation component of the quantities in blue in Figure 9 (e.g., $\overline{U^{\mathbf{bc}}}\,\overline{p^{\mathbf{ha}}}$) are sensitive to the choice of the background stratification, which gives arbitrariness to the quantification of the barotropic and baroclinic HPA fluxes, the PEA flux, and the barotropic and baroclinic buoyancy conversions.

[52] Concerning these disadvantages, Figure C1 provides an explanation for an artificial energy cycle resulting from the sensitivity of the energetics of time mean flows to the choice of the background stratification. There is no such sensitivity in the energetics of waves because $\rho^{\mathbf{a}\prime} = \rho'$ and $p^{\mathbf{ha}\prime} = p^{\mathbf{h}\prime}$. The illustrated distributions of time mean flows and thermocline are idealized for the purpose of this explanation, and nothing to do with the result of the

numerical simulations of tidal flows in the Lombok Strait region.

[53] The red arrows in Figure C1 are time mean overturning circulations which are connected to an open boundary at the right edge of the illustrated domain. The time mean overturning circulations are assumed to be caused by the local balance between the vertical advection and diffusion of density. Namely $\overline{w}\,\overline{\rho}_z = \kappa\overline{\rho}_{zz}$ where κ is the vertical diffusivity associated with either the breaking of high-amplitude internal waves or the hydraulic-jump-like overturning over the sill (shaded black). Note that, at depths slightly above the layer interface, $\overline{\rho}_{zz} > 0$ leads to $\overline{w} < 0$. Likewise, at depths slightly below the layer interface, $\overline{\rho}_{zz} < 0$ leads to $\overline{w} > 0$.

[54] A difference between Figures C1a and C1b is the height of the interface for background stratification (green line), which is associated with the absence and presence of a front on the left of the sill, respectively. While there is no HPA flux in the case of Figure C1a, there is an incoming HPA flux $\int_{-H}^{0} \overline{U}\,\overline{p^{\mathbf{ha}}}dz$ (<0) in the case of Figure C1b. Because this negative HPA flux varies with the choices of the background stratification, the associated energy cycle should be closed by similar quantities. Such an a priori argument suggests an energy cycle as illustrated by Figure C1c using the diagram of Figure 8, that consists of a positive buoyancy conversion $\int\int_{-H}^{0} g\overline{\rho}^{\mathbf{a}}\overline{w}dzdx$ (>0) and an outgoing PEA flux $\int_{-H}^{0} \overline{U}\,(\overline{\rho}^{\mathbf{a}}gz + \rho^{\mathbf{z}}gz + p^{\mathbf{hz}})dz$ (>0). In other words, even if an exact equation for the available potential energy is used instead of the PEA equation, an artificial energy cycle similar to Figure C1c will be reproduced because the mathematical forms of the HPA flux and the buoyancy conversion terms remain the same as that used in the present study.

[55] A conventional way to avoid the above complexity is to look at only the wave correlation component of the baroclinic HPA flux, $\overline{U^{\mathbf{bc}\prime}p^{\mathbf{ha}\prime}}$, while ignoring both the mean correlation component of the baroclinic HPA flux, $\overline{U^{\mathbf{bc}}}\,\overline{p^{\mathbf{ha}}}$, and the overall flux of PE [e.g., NH04; cf. *Warn-Varnas et al.*, 2010]. However CM08 estimated the total component of the baroclinic HPA flux, $\overline{U^{\mathbf{bc}}p^{\mathbf{ha}}}$, without any further decomposition. Note that at least two types of time mean flows are relevant to tidal internal waves, (1) basic geostrophic currents (such as the ITF) and (2) mixing induced overturning circulations (such as the branch of the global conveyor belt). The latter of which is the original process which has long been targeted in the development of the studies of tidal mixing/internal gravity waves in the ocean [*Stommel and Arons*, 1960; *Munk and Wunsch*, 1998], thus is worth recovering in the energy diagnosis of the present study along with the sensitivity study of the ITF. A related discussion appears in section 4.3.

[56] It is clear that the PEA equation (C6) is the cornerstone of our arguments concerning the characteristics of the PEA and HPA fluxes in the presence of time mean flows. The error-free diagnosis of energy quantities and improvement of the energy diagram can only be done on the basis of the exact equations.

C2. Simplified Diagram

[57] The previous energy diagram becomes complicated in the presence of a time mean flow. It would be useful to simplify the diagram by using another equation for PEA which is derived by merging (C12)–(C13), and (C15)

$$\left(\underbrace{L\int_{-H}^{0}\rho^{\mathbf{a}}gzdz}_{\text{PEA}}\right)_t + \left(\underbrace{L\int_{-H}^{0}UMdz}_{\text{MP flux}}\right)_x = L\int_{-H}^{0}\underbrace{U^{\mathbf{bt}}\left(p^{\mathbf{s}}+p^{\mathbf{h}}\right)_x}_{\text{SHPconv(bt)}}dz + L\int_{-H}^{0}\underbrace{U^{\mathbf{bc}}p^{\mathbf{h}}_x}_{\text{HPconv(bc)}}\,dz + L\int_{-H}^{0}gzD^{\rho}dz, \tag{C17}$$

where $M \equiv p^{\mathbf{s}} + p^{\mathbf{h}} + \rho gz$ is the Montgomery potential (MP) [*Montgomery*, 1938; *Andrews*, 1983; *Pedlosky*, 1996] which is defined by the set of ρ and $p^{\mathbf{h}}$, and not the set of $\rho^{\mathbf{a}}$ and $p^{\mathbf{ha}}$. We then consider the time mean of the MP flux and decompose it into three terms

$$\underbrace{\overline{UM}}_{\substack{\text{total}\\ \text{MP flux}}} = \overline{U}\,\overline{M} + \overline{U'M'} = \underbrace{\overline{U}\,\overline{M}}_{\substack{\text{mean}\\ \text{MP flux}}} + \underbrace{\overline{U'^{\mathbf{bt}}M'}}_{\substack{\text{barotropic wave}\\ \text{MP flux}}} + \underbrace{\overline{U'^{\mathbf{bc}}M'}}_{\substack{\text{baroclinic wave}\\ \text{MP flux}}}. \tag{C18}$$

The baroclinic wave MP flux is the sum of the baroclinic wave HPA flux and the baroclinic wave PEA flux: $U'^{\mathbf{bc}}M' = U'^{\mathbf{bc}}p^{\mathbf{ha}\prime} + U'^{\mathbf{bc}}(\rho' gz + p^{\mathbf{hz}})$ so that it includes the effect of the wave advection of potential energy. The set of (C7), (C14), and (C17)–(C18) yields the energy diagram in Figure 10.

[58] This simplified diagram has several advantages and disadvantages. The advantages are as follows: (1) The effect of the energy radiation by internal gravity waves appears only in the baroclinic wave MP flux, and can take into account the effect of finite amplitude waves. (2) The effect of time mean flows appears only in the mean MP flux (and the KE fluxes); the mean MP flux is independent of the choice of $\rho^{\mathbf{z}}$, which gives robustness to the quantification of this term. The disadvantages are as follows: (1) The divergence of the barotropic wave MP flux, which is the source of the energy cycle, is connected to the budget of PEA, which is not suitable for explaining the sequence by which barotropic tidal flows are converted to baroclinic tidal flows or waves. (2) No term in Figure 10 represents the topographic conversion, $g\rho^{\mathbf{a}}w^{\mathbf{bt}}$, in Figure 8.

[59] The energy diagnosis based on the Montgomery potential is compatible with an energy diagnosis in density coordinates [cf. *Aiki and Richards*, 2008]. Integration of the two diagnostic approaches would yield an exact formulation for distinguishing further the budgets of 'mean and wave' energies.

[60] **Acknowledgments.** This paper was improved by comments from two anonymous reviewers. H.A. thanks Yukio Masumoto and Wataru Ohfuchi for encouraging this research; Bach L. Hua and Sylvie L. Gentil for various feedback on the model code; and Yoshihiro Niwa, Katsuro Katsumata, Osamu Isoguchi, and Teruhisa Shimada for useful discussions.

References

Aiki, H., and K. J. Richards (2008), Energetics of the global ocean: The role of layer-thickness form drag, *J. Phys. Oceanogr.*, *38*, 1845–1869, doi:10.1175/2008JPO3820.1.

Aiki, H., and T. Yamagata (2004), A numerical study on the successive formation of Meddy-like lenses, *J. Geophys. Res.*, *109*, C06020, doi:10.1029/2003JC001952.

Aiki, H., K. J. Richards, and H. Sakuma (2011), Maintenance of the mean kinetic energy in the global ocean by the barotropic and baroclinic energy routes, *Ocean Dyn.*, doi:10.1007/s10236-011-0382-y, in press.

Andrews, R. G. (1983), A finite-amplitude Eliassen-Palm theorem in isentropic coordinates, *J. Atmos. Sci.*, *40*, 1877–1883, doi:10.1175/1520-0469(1983)040<1877:AFAEPT>2.0.CO;2.

Baines, P. G. (1982), On internal tide generation models, *Deep Sea Res.*, *29*, 307–338, doi:10.1016/0198-0149(82)90098-X.

Batchelor, G. K. (1967), *An Introduction to Fluid Dynamics*, Cambridge Univ. Press, Cambridge, U. K.

Brandt, P., A. Rubino, W. Alpers, and J. O. Backhaus (1997), Internal waves in the Strait of Messina studied by a numerical model and synthetic apeture radar images from the ERS 1/2 satellites, *J. Phys. Oceanogr.*, *27*, 648–663, doi:10.1175/1520-0485(1997)027<0648:IWITSO>2.0.CO;2.

Buijsman, M. C., Y. Kanarska, and J. C. McWilliams (2010), On the generation and evolution of nonlinear internal waves in the South China Sea, *J. Geophys. Res.*, *115*, C02012, doi:10.1029/2009JC005275.

Carter, G. S., M. A. Merrifield, J. M. Becker, K. Katsumata, M. C. Gregg, D. S. Luther, M. D. Levine, T. J. Boyd, and Y. L. Firing (2008), Energetics of M_2 barotropic-to-baroclinic tidal conversion at the Hawaiian islands, *J. Phys. Oceanogr.*, *38*, 2205–2223, doi:10.1175/2008JPO3860.1.

Chao, S.-Y., D.-S. Ko, R.-C. Lien, and P.-T. Shaw (2007), Assessing the west ridge of Luzon Strait as an internal wave mediator, *J. Oceanogr.*, *63*, 897–991, doi:10.1007/s10872-007-0076-8.

Cummins, P. F., and L. Y. Oey (1997), Simulation of barotropic and baroclinic tides off northern British Columbia, *J. Phys. Oceanogr.*, *27*, 762–781, doi:10.1175/1520-0485(1997)027<0762:SOBABT>2.0.CO;2.

Dukowicz, J. K., and R. D. Smith (1994), Implicit free-surface method for the Bryan-Cox-Semtner ocean model, *J. Geophys. Res.*, *94*, 7991–8014, doi:10.1029/93JC03455.

England, M. H., and F. Huang (2005), On the interannual variability of the Indonesian Throughflow and its linkage with ENSO, *J. Clim.*, *18*, 1435–1444, doi:10.1175/JCLI3322.1.

Ffield, A., and A. L. Gordon (1996), Tidal mixing signatures in the Indonesian seas, *J. Phys. Oceanogr.*, *26*, 1924–1937, doi:10.1175/1520-0485(1996)026<1924:TMSITI>2.0.CO;2.

Helfrich, K. R., and W. K. Melville (2006), Long nonlinear internal waves, *Annu. Rev. Fluid Mech.*, *38*, 395–425, doi:10.1146/annurev.fluid.38.050304.092129.

Holland, W. R. (1975), Energetics of baroclinic oceans, in *Numerical Models of Ocean Circulation*, pp. 168–177, Natl. Acad. of Sci., Washington, D. C.

Jacobson, T., and H. Aiki (2006), An exact energy for TRM theory, *J. Phys. Oceanogr.*, *36*, 558–564, doi:10.1175/JPO2872.1.

Koch-Larrouy, A., G. Madec, D. Iudicone, A. Atmadipoera, and R. Molcard (2008), Physical processes contributing to the water mass transformation of the Indonesian Throughflow, *Ocean Dyn.*, *58*, 275–288, doi:10.1007/s10236-008-0154-5.

Lamb, K. G. (1994), Numerical experiments of internal wave generation by strong tidal flow across a finite amplitude bank edge, *J. Geophys. Res.*, *99*, 843–864, doi:10.1029/93JC02514.

Legg, S., and J. Klymak (2008), Internal hydraulic jumps and overturning generated by tidal flow over a tall steep ridge, *J. Phys. Oceanogr.*, *38*, 1949–1964, doi:10.1175/2008JPO3777.1.

Masumoto, Y., and T. Yamagata (1996), Seasonal variaions of the Indonesian Throughflow in a general ocean circulation model, *J. Geophys. Res.*, *101*, 12,287–12,293, doi:10.1029/95JC03870.

Matthews, J. P., H. Aiki, S. Masuda, T. Awaji, and Y. Ishikawa (2011), Monsoon regulation of Lombok Strait internal waves, *J. Geophys. Res.*, doi:10:1029/2010JC006403, in press.

Menesguen, C., B. L. Hua, C. Papenberg, D. Klaeschen, L. Geli, and R. Hobbs (2009), Effect of bandwidth on seismic imaging of rotating stratified turublence surrounding an anticyclonic eddy from field data and numerical simulations, *Geophys. Res. Lett.*, *36*, L00D05, doi:10.1029/2009GL039951.

Mitnik, L., W. Alpers, and H. Lim (2000), Thermal plumes and internal solitary waves generated in the Lombok Strait studied by ERS SAR, in *ERS-Envisat Symposium: Looking Down to Earth in the New Milenium 16–20 October 2000*, vol. SP-461, pp. 1–9, Eur. Space Agency, Paris.

Miyata, M. (1985), An internal solitary wave of large amplitude, *La Mer*, *23*, 43–48.

Montgomery, R. B. (1938), *Circulation in Upper Layers of Southern North Atlantic Deduced With the Use of Isentropic Analysis*, *Pap. Phys. Oceanogr. Meteorol. Ser.*, vol. 6, Mass. Inst. of Technol., Woods Hole Oceanogr. Inst., Cambridge, Mass.

Moum, J. N., J. D. Nash, and J. M. Klymak (2008), Small-scale processes in the coastal ocean, *Oceanography*, *21*, 22–33.

Munk, W., and C. Wunsch (1998), Abyssal recipes II: Enegetics of tidal and wind mixing, *Deep Sea Res.*, *45*, 1997–2010, doi:10.1016/S0967-0637(98)00070-3.

Murray, S. P., and D. Arief (1988), Throughflow into the Indian Ocean through the Lombok Strait, January 1985–January 1986, *Nature*, *333*, 445–447, doi:10.1038/333444a0.

Nash, J. D., and M. H. Alford (2005), Estimating internal wave energy fluxes in the ocean, *J. Atmos. Oceanic Tech.*, *22*, 1551–1570, doi:10.1175/JTECH1784.1.

Ningsih, N. S., R. Rachmavani, S. Hadi, and I. S. Brodjonegoro (2008), Internal waves dynamics in the Lombok Strait studied by a numerical model, *Int. J. Remote Sens. Earth Sci.*, *5*, 17–33.

Niwa, Y., and T. Hibiya (2004), Three-dimensional numerical simulation of M2 internal tides in the East China Sea, *J. Geophys. Res.*, *109*, C04027, doi:10.1029/2003JC001923.

Osborne, A. R., and T. L. Burch (1980), Internal solitons in the Andaman Sea, *Science*, *208*, 451–460, doi:10.1126/science.208.4443.451.

Pedlosky, J. (1996), *Ocean Circulation Theory*, 453 pp., Springer, Berlin.

Robertson, R. (2010), Tidal currents and mixing at the INSTANT mooring locations, *Dyn. Atmos. Oceans*, *50*, 331–373, doi:10.1016/j.dynatmoce.2010.02.004.

Robertson, R., and A. Ffield (2008), Baroclinic tides in the Indonesian seas: Tidal fields and comparison to observations, *J. Geophys. Res.*, *113*, C07031, doi:10.1029/2007JC004677.

Shen, C. Y., T. E. Evans, R. M. Oba, and S. Finette (2009), Three-dimensional hindcast simulation of internal soliton propagation in the Asian Seas International Acoustics Experiment area, *J. Geophys. Res.*, *114*, C01014, doi:10.1029/2008JC004937.

Smagorinsky, J. (1963), General circulation experiments with the primitive equation. Part I. The basic experiment, *Mon. Weather Rev.*, *91*, 99–165, doi:10.1175/1520-0493(1963)091<0099:GCEWTP>2.3.CO;2.

Small, J., and J. Martin (2002), The generation of non-linear internal waves in the Gulf of Oman, *Cont. Shelf Res.*, *22*, 1153–1182, doi:10.1016/S0278-4343(01)00094-2.

Sprintall, J., S. E. Wijffels, R. Molcard, and I. Jaya (2009), Direct estimates of the Indonesian Throughflow entering the Indian Ocean: 2004–2006, *J. Geophys. Res.*, *114*, C07001, doi:10.1029/2008JC005257.

Stommel, H., and A. B. Arons (1960), On the abyssal circulation of the World Ocean. Part I: Stationary planetary flow patterns on a sphere, *Deep Sea Res.*, *6*, 140–154.

Susanto, R. D., L. Mitnik, and Q. Zheng (2005), Waves observed in the Lombok Strait, *Oceanography*, *18*, 80–87.

Warn-Varnas, A. C., S. A. Chin-Bing, D. B. King, J. A. Hawkins, K. G. Lamb, and M. Teixeria (2005), Yellow Sea ocean-acoustic solitary wave modeling studies, *J. Geophys. Res.*, *110*, C08001, doi:10.1029/2004JC002801.

Warn-Varnas, A. C., J. Hawkins, K. G. Lamb, S. Piacsek, S. Chin-Bing, D. King, and G. Burgos (2010), Solitary wave generation dynamics at Luzon Strait, *Ocean Modell.*, *31*, 9–27, doi:10.1016/j.ocemod.2009.08.002.

Zheng, Q., R. D. Susanto, C.-R. Ho, Y. T. Song, and Q. Xu (2007), Statistical and dynamical analyses of generation mechanisms of solitary internal waves in the northern South China Sea, *J. Geophys. Res.*, *112*, C03021, doi:10.1029/2006JC003551.

H. Aiki, Research Institute for Global Change, Japan Agency for Marine-Earth Science and Technology, 3173-25 Showamachi, Kanazawa-ku, Yokohama 236-0001, Japan. (aiki@jamstec.go.jp)

K. G. Lamb, Department of Applied Mathematics, University of Waterloo, Waterloo, ON N2L 3G1, Canada.

J. P. Matthews, Environmental Satellite Applications, Llys Awel, Mount Street, Menai Bridge, Anglesey Wales, LL59 5BW, UK.